Impact of topography on black carbon transport to the southern Tibetan Plateau during pre-monsoon season and its climatic implication

[1]Meixin Zhang, [1]Chun Zhao*, [2,3]Zhiyuan Cong, [1]Qiuyan Du, [1]Mingyue Xu, [1]Yu Chen, [4]Ming Chen, [1]Rui Li, [1]Yunfei Fu, [1]Lei Zhong, [3,5]Shichang Kang, [6]Delong Zhao, [6]Yan Yang

[1]School of Earth and Space Sciences, University of Science and Technology of China, Hefei, China

[2]Key Laboratory of Tibetan Environment Changes and Land Surface Processes, Institute of Tibetan Plateau Research, Chinese Academy of Sciences (CAS), Beijing 100101, China

[3]CAS Center for Excellence in Tibetan Plateau Earth Sciences, Institute of Tibetan Plateau Research, CAS, Beijing 100101, China

[4]National Center for Atmospheric Research, Boulder, CO, USA

[5]State Key Laboratory of Cryosphere Science, Northwest Institute of Eco-Environment and Resources, CAS, Lanzhou 730000, China

[6]Beijing Weather Modification Office, Beijing 100101, China

Manuscript for submission to Atmos. Chem. Phys.

*Corresponding author: Chun Zhao (chunzhao@ustc.edu.cn)

Key points:

1. The black carbon (BC) transport across the Himalayas can overcome a majority of mountain ridges, but the valley transport is much more efficient.

2. The complex topography results in stronger overall crossing-Himalayas transport primarily due to the enhanced valley wind, deeper valley channels, and induced small-scale favorable circulation.

3. The complex topography generates 50% higher transport flux of BC across the Himalayas and 30-50% stronger BC radiative heating in the atmosphere up to 10 km over the Tibetan Plateau (TP) than that with the smoother topography, which implies that global climate models with relatively coarse resolution may introduce significant negative biases in estimating BC radiative forcing over the TP due to smooth topography.

4. The different topography also leads to different distributions of snow cover and BC forcing in snow over the TP.

Abstract

Most of previous modeling studies about black carbon (BC) transport and impact over the Tibetan Plateau (TP) conducted simulations with horizontal resolutions coarser than 10 km that may not be able to resolve well the complex topography of the Himalayas. In this study, the two experiments covering entire Himalayas with the Weather Research and Forecasting Model coupled with chemistry (WRF-Chem) at the horizontal resolution of 4 km but with two different topography datasets (4-km complex topography and 20-km smooth topography) are conducted for pre-monsoon season (April, 2016) to investigate the impacts of topography on modeling the transport and distribution of BC over the TP. Both experiments show evident accumulation of aerosols near the southern Himalayas during the pre-monsoon season, consistent with the satellite retrievals. The observed episode of high surface BC concentration at the station near the Mt. Everest due to heavy biomass burning near the southern Himalayas is well captured by the simulations. The simulations indicate that the prevailing up-flow across the Himalayas driven by the large-scale circulation during the daytime is the dominant transport mechanism of South Asian BC into the TP, and is much stronger than that during the nighttime. The simulation with 4-km topography resolves more valleys and mountain ridges, and shows that the BC transport across the Himalayas can overcome a majority of mountain ridges but the valley transport is more efficient. The complex topography results in stronger overall crossing-Himalayas transport primarily due to the enhanced valley wind, deeper valley channels, and induced small-scale favorable circulation. This results in 50% higher transport flux of BC across the Himalayas and 30-50% stronger BC radiative heating in the atmosphere up to 10 km over the TP from the simulation with 4-km complex topography than that with 20-km smoother topography. The different topography also leads to different distributions of snow cover and BC forcing in snow. This study implies that global climate models generally with even coarser resolutions than 20 km and therefore relatively smoother topography may introduce significant negative biases in estimating light absorbing aerosol radiative forcing over the TP.

1. Introduction

The Tibetan Plateau (TP) is the highest plateau in the world with an average elevation over 4 km and an area of approximately 2.5×10^6 km^2, known as the world's third pole (Qiu, 2008), and its enormous dynamic and thermal effects have a huge impact on large-scale atmospheric circulation through the energy exchange with the atmosphere especially the troposphere, such as Asian monsoon (e.g., Ye and Wu, 1998; Duan and Wu, 2005; Wu et al., 2007, 2012; Boos and Kuang, 2013; Chen and Bordoni, 2014; He et al., 2019; Zhao et al., 2019). In addition, the glacial melting water of TP is one of the important sources of water resources of the Indus River, Ganges River, Yangtze River, and Yellow River in Asia (e.g., Singh and Bengtsson, 2004; Barnett et al., 2005; Immerzeel et al., 2010; Lutz et al., 2014). Previous studies found aerosols in the atmosphere over/around the TP could change the regional climate of Asia (e.g., Qian et al., 2011, 2015; Lau et al., 2017, 2018). Model simulations showed that the absorptive aerosols changed the surface radiative flux over the TP by 5-25 W m^{-2} during the pre-monsoon season in April and May and led to the changes in summer monsoon circulations (Qian et al., 2011). Meanwhile, aerosol may affect the atmosphere by modulating the vertical structure of cloud and precipitation around the TP, and thus change the distribution of atmospheric latent heat around the TP, which is the main driving force of regional atmosphere circulations (e.g., Li et al., 2010, 2017, 2019). Moreover, when absorbing aerosols settle on the snow-covered areas, they will blacken the surface of snow cover and glacier to a large extent (e.g., Hansen and Nazarenko, 2004; Ramanathan and Carmichael, 2008; Lau et al., 2010, 2018; Lee et al., 2013; Zhang et al., 2017, 2018), reduce the snow albedo so as to absorb more solar radiation and cause the consequences of accelerated melting (e.g., Ramanathan et al., 2007; Ming et al., 2009; Yasunari et al., 2010; Ji et al., 2015; Zhang et al., 2015). According to the Intergovernmental Panel on Climate Change Fifth Assessment Report (IPCC AR5), the radiative forcing caused by the important component of absorbing aerosols, black carbon (BC), on the surface snow is 0.04 W m^{-2} (0.02-0.09 W m^{-2}) on global average, and the regional forcing (such as over the Arctic and the Himalayas) can be considerably large.

The TP is surrounded by various sources of pollutants. Over the South of TP, previous studies have suggested that South Asia was the main source of pollutants transported to the plateau (e.g., Cong et al., 2009, 2015a, b; Kopacz et al., 2011; Lu et al., 2012; Zhao et al., 2013; Wang et al., 2015; Zhang et al., 2015; Kang et al., 2015; Li et al., 2016; Chen et al., 2018; Kang et al., 2019). A huge blanket or layer of "haze" composes of light-absorbing carbonaceous

103 aerosol particles that often erupts in the pre-monsoon season over South Asia and has a
104 significant influence on the plateau (e.g., Prasad and Singh, 2007; Engling and Gelencser,
105 2010). Among them, biomass burning emission reaching the maximum in pre-monsoon season
106 over South Asia is one of the dominant sources (e.g., Cong et al., 2015b). Many studies
107 investigated the transport mechanisms of South Asian pollutants to the TP and found that the
108 pollutants transported across the Himalayas were mainly due to the combination of large-scale
109 circulation and regional wind (e.g., Hindman and Upadhyay, 2002; Cao et al., 2010; Dumka et
110 al., 2010; Marinoni et al., 2010; Cong et al., 2015a; Kang et al., 2015; Lüthi et al., 2015; Zhang
111 et al., 2017). Cong et al. (2015a) conducted seven-day backward air-mass trajectories
112 experiment and found strong westerly passed through western Nepal, northwest India and
113 Pakistan (i.e., southern Himalayas) in the pre-monsoon season. Dumka et al. (2010) and Kang
114 et al. (2015) inferred from the trajectory analysis that long-distance transport from Africa and
115 Europe may also affect the BC concentration of Himalayas in addition to the influence of
116 regional pollution.

117 Although previous studies have confirmed the transport of pollutants across the Himalayas,
118 the complex topography of Himalayas complicates transport mechanisms. On one hand, Cao
119 et al. (2010) revealed that the Himalayas acted as a huge barrier to the transport of a large
120 amount of BC over the plateau based on model simulations. On the other hand, some studies
121 found that the valleys across the Himalayas served as channels for efficient transport of
122 pollutants (e.g., Hindman and Upadhyay, 2002; Marinoni et al., 2010). Marinoni et al. (2010)
123 analyzed the observation of wind at a station of the southern Himalayas and found that a distinct
124 valley wind system with the prominent southerly continuously transported pollutants to the
125 plateau. Most of these studies used observations and back-trajectory models to demonstrate the
126 transport pathways of pollutants to the TP, which cannot explicitly reveal the transport
127 mechanisms underneath, in particular quantifying the impacts of complex topography.

128 A few of modeling studies investigated the pollutant transport mechanisms using 3-D
129 chemical transport models (e.g., Kopacz et al., 2011; Liu et al., 2015; Zhang et al., 2017; Yang
130 et al., 2018). However, most of them simulated transport processes at relatively coarse
131 horizontal resolutions (e.g., 20-100 km), which cannot resolve well the complex topography of
132 Himalayas. It is noteworthy that studies about the aerosol climatic impact over the TP also used
133 climate models at relatively coarse horizontal resolutions (e.g., Flanner and Zender, 2005;
134 Menon et al., 2010; Kopacz et al., 2011; Qian et al., 2011, 2015; He et al., 2014; Zhang et al.,
135 2015; Ji et al., 2016). So far, there is only one study that used a chemical transport model at a
136 horizontal resolution of sub-10 km to investigate pollutant transport mechanisms over the

eastern Himalayas (Cao et al., 2010). Furthermore, none of studies assessed quantitatively the impacts of topography on modeling the pollutant transport across the Himalayas and hence on estimating aerosol distribution and radiative forcing over the TP.

In order to examine the potential impacts of complex topography on pollutant transport across the Himalayas over the TP, this study conducts multiple experiments with the Weather Research and Forecasting Model coupled with chemistry (WRF-Chem, Grell et al., 2005; Skamarock et al., 2008). The WRF-Chem model is selected because it includes the interaction between meteorology and aerosol and is widely used for regional modeling of aerosol and its climatic impact (e.g., Cao et al., 2010; Zhao et al., 2010, 2011, 2012, 2014; Wu et al., 2013; Gao et al., 2014; Huang et al., 2015; Fan et al., 2015; Feng et al., 2016; Zhong et al., 2017; Sarangi et al., 2019; Liu et al., 2020). The model has also been used to investigate the aerosol transport and climatic impact over the Himalayas region (e.g., Feng et al., 2016; Cao et al., 2010; Sarangi et al., 2019). The model is suitable for simulations at hydrostatic and non-hydrostatic scales and thus can be used for investigating the impacts of resolution-dependent feature, such as topography, on modeling results. In particular, the meteorological part of the model (WRF) has been systematically evaluated and used to investigate the impacts of resolutions on simulations of moisture transport and climate over the Himalayas region (e.g., Shi et al., 2008; Karki et al., 2017; Lin et al., 2018). All of these previous studies with the model lay the foundation for this modeling study.

Two experiments with different topography representations are conducted to investigate the impacts of topography complexity on the pollutant transport across the Himalayas and the resulting radiative forcing over the TP. The simulations are conducted for April 2016 in pre-monsoon season, because South Asia is seriously polluted during this period and the pollutants transported to the TP during the period may have significant impacts on Asian monsoon system (e.g., Lau et al., 2006a, b; Ding et al., 2009; Kuhlmann and Quaas, 2010; Qian et al., 2011, 2015). In addition, the observed concentration of BC at the observation station besides Mt. Everest shows an evident pollution episode from April 5th to 16th of 2016, deserving the investigation of the transport mechanisms. The rest of the paper is organized as follows. Section 2 describes briefly the WRF-Chem model, the physics parameterizations, and the model configuration for this study, followed by a description of data for evaluation. The series of numerical experiments at different resolutions are analyzed in Section 3. The findings are then summarized and discussed in Section 4.

2. Methodology

2.1 Model and experiments

2.1.1 WRF-Chem model

In this study, the version of WRF-Chem updated by University of Science and Technology of China (USTC version of WRF-Chem) is used. This USTC version of WRF-Chem includes some additional capabilities such as the diagnosis of radiative forcing of aerosol species, land surface coupled biogenic volatile organic compound (VOC) emission, aerosol-snow interaction compared with the publicly released version (Zhao et al., 2013a, b, 2014, 2016; Hu et al., 2019; Du et al., 2020). The Model for Simulating Aerosol Interactions and Chemistry (MOSIAC) (Zaveri et al., 2008) and the Carbon Bond Mechanism-Z (CBM-Z) gas phase mechanisms (Zaveri and Peters, 1999) are selected. The MOSAIC aerosol scheme uses an approach of segmentation to represent aerosol size distribution with four or eight discrete size bins (Fast et al., 2006). It consists of a range of physical and chemical processes such as nucleation, condensation, coagulation, aqueous phase chemistry, and water uptake by aerosol. The parameterization of dry deposition of aerosol mass and number is according to the method of Binkowski and Shankar (1995), including particle diffusion and gravitational effects. Aerosol-cloud interactions were included in the model by Gustafson et al. (2007) for calculating the activation and re-suspension between dry aerosols and cloud droplets. The wet removal of grid-resolved stratiform clouds/precipitation includes two aspects, namely in-cloud removal (rainout) and below-cloud removal (washout) by Easter et al. (2004) and Chapman et al. (2009), respectively. Aerosol optical properties such as single scattering albedo (SSA) and scattering asymmetry and so on are calculated at each model grid through the function of wavelength. The shortwave (SW) and longwave (LW) refractive indices of aerosols use the Optical Properties of Aerosols and Clouds (OPAC) data set (Hess et al., 1998), with a detailed description of the computation of aerosol optical properties can be found in Barnard et al. (2010) and Zhao et al. (2013a). For both short wave and long wave radiation, aerosol radiation feedback combined with the Rapid Radiative Transfer Model (RRTMG) (Mlawer et al., 1997; Iacono et al., 2000) was implemented by Zhao et al (2011). For the diagnosis of the optical properties and direct radiative forcing of various aerosol species in the atmosphere, the method described by Zhao et al (2013a) is adopted. The radiative forcing of light absorbing aerosol in surface snow is estimated with the Snow, Ice, and Aerosol Radiative model (SNICAR) (Flanner and Zender, 2005) in the land surface scheme as introduced by Zhao et al. (2014).

202 More details about the coupling between the WRF-Chem and SNICAR models can be found

203 in Zhao et al. (2014).

204 2.1.2 Numerical experiments

205   In this study, the WRF-Chem simulations are performed with two nested domains (one-

206 way nesting), one outer domain at 20 km horizontal resolution with 350×250 grid cells (62°E

207 -112°E, 1°N -38°N) and one inner domain at 4 km horizontal resolution with 400×300 grid

208 cells (75°E -92°E, 23°N -35°N) (Fig. 1). The inner domain roughly covers the entire Himalayas.

209 The WRF-Chem simulations conducted in this study use the terrain following coordinate

210 (Skamarock et al., 2008). To resolve the vertical structure of transport across the Himalayas,

211 the simulations are configured with 54 vertical layers and denser layers near the surface. For

212 example, averaged over a region (26°N-28°N, 76°E-80°E) near the southern Himalayas, there

213 are about 17 layers below 2 km above the ground (Fig. 2). The goal of this study is to investigate

214 the impacts of different representations of topography on the transport of BC across the

215 Himalayas. Therefore, besides this control experiment, one sensitivity experiment is also

216 conducted with the same configuration as the control one except that the topography of the

217 inner domain at 4 km resolution is prescribed to follow that at 20 km resolution similar as

218 previous studies (e.g., Shi et al., 2008; Wu et al., 2012; Lin et al., 2018). More specifically, the

219 sensitivity experiment applies a single value for each nested 5×5 grids over the inner domain

220 as the corresponding grid of 20 km over the outer domain. The two experiments are referred to

221 the simulations with complex and smooth topography, respectively, hereafter. Fig. 3 shows the

222 spatial distribution of terrain height over the inner domain with complex (4-km dataset) and

223 smooth (20-km dataset) topography. It is evident that the terrain is much smoother from the

224 20-km dataset than from the 4 km dataset. The mountain ridges and valleys can be resolved to

225 some extent in the 4-km dataset but mostly missed or underestimated at 20-km. The probability

226 distributions of terrain height from the 20-km and 4-km datasets (Fig. S1 in the supporting

227 material) show that the difference between the two datasets is small for the terrain height lower

228 than ~4.5 km but is significant for the terrain height above ~4.5 km. The difference of results

229 from the two experiments over the inner domain is analyzed as the impacts of topography

230 representations. Therefore, all the results shown below are from the simulations of the inner

231 domain at 4 km resolution with different topography if not otherwise stated.

232   The simulations are conducted for March 29th-April 20 of 2016 for the reason as discussed

233 in the introduction. The results of April 1th-20th are analyzed for the observed pollution episode

234 to allow a few days spin-up for chemical initial condition. The meteorological initial and lateral

235   boundary conditions are derived from the European Centre for Medium-Range Weather

236   Forecasts (ECMWF) reanalysis data at 0.5°×0.66° horizontal resolution and 6 h temporal

237   intervals (ERA-Interim dataset). The modeled u and v component wind, atmospheric

238   temperature, and geopotential height over the outer domain are nudged towards the reanalysis

239   data with a nudging timescale of 6 h following previous studies (e.g., Stauffer and Seaman,

240   1990; Seaman et al., 1995; Liu et al., 2012; Zhao et al., 2014; Karki et al., 2017; Hu et al., 2016,

241   2020). Spectral nudging method is applied to balance the performance of simulation at the large

242   and small scales (Liu et al., 2012), and only to the layers above the planetary boundary layer

243   (PBL) with nudging coefficients of 3×10^{-4} s^{-1}. A wave number of three is selected for both

244   south-north and west-east directions. Please note that the choices of nudging coefficients and

245   wave numbers for spectral nudging in this study are empirical. The purpose of nudging is to

246   simulate reasonably large-scale feature so that small-scale impacts from the complex

247   topography can be focused. Therefore, the modeling sensitivity to these choices is not tested in

248   this study. The results show that the simulations with nudging method can reproduce the large-

249   scale circulation at 700 hPa and higher over the outer domain compared to the reanalysis dataset

250   with the spatial correlation coefficient of 0.96-0.98.

251   The Mellor-Yamada-Nakanishi-Niino (MYNN) planetary boundary layer scheme

252   (Nakanishi and Niino, 2006), Community Land Model (CLM) land surface scheme (Oleson et

253   al., 2010), Morrison 2-moment microphysics scheme (Morrison et al., 2009), Kain-Fritsch

254   cumulus scheme (Kain, 2004), and Rapid Radiative Transfer Model (RRTMG) longwave and

255   shortwave radiation schemes (Iacono et al., 2000) are used in this study. The chemical initial

256   and boundary conditions are provided by a quasi-global WRF-Chem simulation for the same

257   time period to include long-range transported chemical species. The quasi-global WRF-Chem

258   simulation is performed at 1°×1° horizontal resolution using a quasi-global channel

259   configuration with 360×130 grid cells (180°W-180°E, 60°S-70°N). More details about the

260   general configuration of quasi-global WRF-Chem simulation can be found in Zhao et al.

261   (2013b) and Hu et al. (2016). The detailed configuration of WRF-Chem experiments is

262   summarized in Table 1. Due to the lack of publicly available in-situ observations, this study

263   does not tend to evaluate systematically the simulated meteorological fields over the Himalayas

264   region. However, as shown in Table 1, the choice of physical parameterizations in this study

265   follows that of one previous study (Karki et al., 2017) that evaluated systematically the WRF

266   simulation for one entire year over the Himalayas region. Their results showed that the WRF

267   simulation at convection-permitting scale could generally capture the essential features of

268 meteorological fields such as precipitation, temperature, and wind over the Himalayas region.
269 Therefore, the WRF-Chem simulations in this study are reliable to investigate the impacts of
270 topography over the Himalayas region.

271 2.1.3 Emissions

272 Anthropogenic emissions for outer and inner simulation domains are obtained from the
273 Hemispheric Transport of Air Pollution version-2 (HTAPv2) at $0.1°×0.1°$ horizontal resolution
274 and a monthly temporal resolution for year 2010 (Janssens-Maenhout et al., 2015), except that
275 emissions of East Asia are from the MIX Asian anthropogenic emission inventory at $0.1°×0.1°$
276 horizontal resolution for 2015 (Li et al., 2017). Biomass burning emissions are obtained from
277 the Fire Inventory from National Center for Atmospheric Research (FINN) with hourly
278 temporal resolution and 1 km horizontal resolution (Wiedinmyer et al., 2011) for the simulation
279 period, and are vertically distributed following the injection heights suggested by Dentener et
280 al. (2006) from the Aerosol Comparison between Observations and Models (AeroCom) project.
281 Sea-salt emission follows Zhao et al. (2013b), which includes correction of particles with
282 radius less than 0.2 μm (Gong, 2003) and dependence of sea-salt emission on sea surface
283 temperature (Jaeglé et al., 2011). The vertical dust fluxes are calculated with the Georgia
284 Tech/Goddard Global Ozone Chemistry Aerosol Radiation and Transport (GOCART) dust
285 emission scheme (Ginoux et al., 2001), and the emitted dust particles are distributed into the
286 MOSAIC aerosol size bins following a theoretical expression based on the physics of scale-
287 invariant fragmentation of brittle materials derived by Kok (2011). More details about the dust
288 emission scheme coupled with MOSAIC aerosol scheme in WRF-Chem can be found in Zhao
289 et al. (2010, 2013b).

290 As shown in Fig. 1, anthropogenic fossil fuel emissions of BC are high over Northeast
291 India. The fossil fuel BC emissions over Nepal, the country nearby the southern Himalayas,
292 are relatively low. Instead, biomass burning emissions of BC are extremely high in Nepal and
293 Northwest India (South Himalayas, 26°N-29°N). Averaged over the South Himalayas of inner
294 domain that may significantly affect the pollutant transport into the TP, the biomass burning
295 emissions of BC are much higher than its anthropogenic fossil fuel emissions, particularly for
296 the pollution episode (Fig. 4). The anthropogenic BC emissions are set constant through April,
297 while biomass burning emissions show a strong fire event in April 5-16. During the event, the
298 biomass burning BC emissions can be close to a factor of 2 of the anthropogenic fossil fuel BC
299 emissions over South Himalayas.

300

301 **2.2 Dataset**

302   Three datasets are used to compare with the modeling results to demonstrate the pollutant
303   episode and spatial distribution. One is from the Moderate Resolution Imaging
304   Spectroradiometer (MODIS) instruments on Aqua and Terra satellites. The MODIS Aerosol
305   Product monitors the ambient aerosol optical thickness over the oceans globally and over the
306   continents. Daily Level 2 Aerosol Optical Depth (AOD) at 550 nm products with the spatial
307   resolution of 10 km×10 km (at nadir) from both Aqua and Terra are applied. When compared
308   with the modeling results, the simulations are sampled at the satellite overpass time and
309   location. The second one is from the Aerosol Robotic Network (AERONET) (Holben et al.,
310   1998) that has ~100 similar globally distributed sun and sky scanning ground-based automated
311   radiometers, which provide measurements of aerosol optical properties throughout the world
312   (Dubovik and King, 2000; Dubovik et al., 2002). In this study, AERONET measured AOD at
313   675 nm and 440 nm from two sites over the TP, Qomolangma site (QOMS, 86.94°E, 28.36°N)
314   and Namco site (NAM, 90.96°E, 30.77°N) are used to derive the AOD at 550 nm (using the
315   Angström exponent) for comparison with modeling results at 550 nm. All of the retrievals of
316   AOD are at quality level 2, and the uncertainty of AOD measurements is about 0.01 (Holben
317   et al., 2001). In this study, the available data in April 2016 are used to evaluate the modeling
318   results during the same period.

319   The third one is the measurement of surface BC mass concentration collected during the
320   simulation period for April 4-20 of 2016 at the Qomolangma (Mt. Everest) Station for
321   Atmospheric and Environmental Observation and Research, Chinese Academy of Sciences
322   (QOMS, 86.94°E, 28.36°N) which is located at the northern slope of the Himalayas, about
323   4276 meters above sea level. The BC mass concentration is measured with the widely-used
324   instrument Aethalometer (AE-33) that can provide real-time BC mass concentration
325   measurements. The calibration of air flow is routinely conducted to maintain the data quality.
326   The instrument estimates the BC mass concentration based on the optical method through
327   measuring the reduction in light intensity induced by BC. The method assumes that the
328   relationship between attenuation and BC surface loading is linear for low attenuation values.
329   However, this relationship becomes nonlinear when the attenuation values are high due to a
330   filter saturation effect, which may lead to underestimation of the high BC concentration. The
331   detection limit of AE-33 instrument is 5 ng/m^3, and the uncertainty is estimated to be within
332   10% (e.g., Chen et al., 2018; Bansal et al., 2019; Kant et al., 2019). The dataset of BC mass
333   concentration used in this study was reported by Chen et al., (2018), where more details about
334   the measurements can be found.

3. Results

3.1 Spatial distribution of BC around the TP

Figure 5 shows the spatial distributions of column integrated BC mass within the inner domain from the simulations at 4 km resolution with complex and smooth topography averaged for April 1-20, 2016, and the difference between the two is also shown. For both experiments, the southern Himalayas is an apparent boundary line for the distribution of BC with a sharp gradient across the Himalayas. The high BC mass loading exists near the southern Himalayas reaching over 10 mg/m^2, which is largely contributed by the biomass burning emissions during the period (Fig. 4), while the value reduces significantly to less than 0.4 mg/m^2 over the TP. In general, the column BC mass loading from the simulation with complex topography is higher over the TP and lower over the region to the south of Himalayas compared with the smooth topography. Figure 6 displays the spatial distributions of AOD from the MODIS retrievals and the simulations at 4 km with two different topography averaged for April 1-20, 2016. In general, both simulations reproduce the overall spatial distribution of AOD, with the large values near the southern Himalayas, consistent with the BC mass loading. The difference between the simulations and retrievals may be partly related to the uncertainties in emissions particularly for biomass burning emissions. Other than intense emissions, the wind circulation around the TP may also play an important role in accumulating BC near the southern Himalayas. Because of the block of Himalayas, the wind circulation at 500 hPa is divided into two branches as westerly and northwesterly. Both of them are relatively dry airflows with little effect on pollutant removal, favor the accumulation of pollutants near the southern Himalayas, and carry the pollutants to the TP (e.g., Dumka et al., 2010; Kang et al., 2015; Cong et al., 2015a).

The AOD retrieved at two AERONET sites over the TP are compared with the two simulations for April 1-20, 2016 (Fig. 7). The AOD at the QOMS site near the northern Himalayas is higher than that at the NAM site inside of the TP. Both simulations can capture this gradient. The simulation with complex topography produces higher AOD than does the one with smooth topography at both sites. The modeling biases (normalized mean bias, NMB) reduce from -46% (smooth topography) to 9% (complex topography) at the QOMS site and from -26% (smooth topography) to -10% (complex topography) at the NAM site. Although the correlation coefficient between the simulations and observation increases from 0.37 (smooth topography) to 0.53 (complex topography) at the QOMS site, it is similar (~0.2) between the two simulations at the NAM site. The correlation coefficient is higher at the QOMS site near the source region than the NAM site farther away, which may indicate the model processes

368   affecting the transport over the TP still need examination with more observations. The NAM

369   site over the eastern TP may also be affected by other sources that are not counted in this study.

370   The modeling of temporal variations of pollutants over the TP deserves further investigation

371   with more observations.

372   There is one in-situ observational station (QOMS) near the Mt. Everest (black dot shown

373   in Fig. 1) to collect the surface BC concentration. The observed surface BC concentration at

374   this station is compared with the corresponding simulations for this period as shown in Figure

375   8. Without local emission source, the surface BC concentration at QOMS is primarily

376   contributed by the transport. The temporal variation of observed surface BC concentration

377   correlates highly with the biomass burning emissions as shown in Fig. 4, with the peak value

378   on April 11 reaching ~3 ug/m^3. One sensitivity experiment without biomass burning emissions

379   shows that the simulated BC concentration at QOMS will be significantly reduced without the

380   peak (not shown), which further proves that the BC concentration over the northern Himalayas

381   can be largely influenced by the pollution episode near the southern Himalayas. It is noteworthy

382   that both simulations can reproduce the episode in time and magnitude, and the difference at

383   this station is small. The spatial distribution of difference in surface BC concentration between

384   the two simulations (Fig. S2) is more heterogeneous than that of column BC mass (Fig. 5),

385   reflecting the impact of topography on transport (see the discussion in Section 3.2).

386

387   **3.2 Transport flux into the TP**

388   To further understand the difference in BC surface concentration and column mass loading

389   over the TP between the two simulations with different topography, Figure 9 shows the

390   longitude-height cross section of BC transport flux along the cross line (shown as the black

391   dash line in Fig. 3) from the two simulations at local time (LT) 03:00 and 15:00 averaged for

392   April 1-20 to represent nighttime and daytime transport, respectively. The PBL height along

393   the cross line is also shown as the black dash line. The transport flux is calculated by projecting

394   the wind field perpendicularly to the cross line and then multiplying the BC mass concentration

395   along the cross line. More specifically, the transport flux is calculated as following:

$$\mathrm{TF} = C * (u * \sin\alpha + v * \sin\beta) \qquad (1)$$

397   Where α is the angle between east-west wind component and the cross line, β is the angle

398   between south-north wind component and the cross line, and C is the BC mass concentration

399   at the grid along the cross line. The flux is estimated at each model level. Positive values

400   represent the transport towards the TP, while negative values represent the transport away from

401 the TP. It is evident that BC is imported into the TP during the day and night on the west of
402 ~85°E, although the transport flux is much larger during the daytime than nighttime. On the
403 east of ~85°E, BC is imported into the TP during the day but exported slightly from the TP
404 during the night. The difference of transport flux between on the west and east of ~85°E is
405 primarily due to the influence of large-scale westerly that is relatively weak on the east of
406 ~85°E compared with the west (Fig. 5). If removing the mean flux during the simulation period,
407 the transport flux anomalies show evident diurnal variation between the day and night (Fig. S3
408 in the supporting material). This suggests that on average, the large-scale westerly is one of the
409 key mechanisms transporting BC across the Himalayas into the TP, while the circulation
410 anomalies strengthen the prevailing import transport during the daytime and weaken the import
411 during the night, particularly in the west of ~85°E. The strong transport is primarily within the
412 PBL during the daytime, and the deeper PBL during the daytime allows BC over the source
413 region mixed to higher altitude, which also leads to stronger import transport during the day
414 than the night.

415   The difference between the simulations with two different topography is evident. The
416 mountain ridges are much higher and valleys are much deeper with the complex topography
417 than with the smooth topography. The simulation with smooth topography produces
418 overwhelming crossing-Himalayas transport towards the TP within the PBL, in particular
419 during the daytime. Although, in the simulation with complex topography, the mountain ridges
420 resolved weaken the crossing-Himalayas transport compared to the simulation with smooth
421 topography, the overall positive values near the surface indicate that the transport can overcome
422 most mountain ridges along the Himalayas. The transport fluxes near the surface from the
423 simulation with complex topography become close-to-zero only at a few mountain ridges that
424 are 6.5 km or higher. To better demonstrate the transport pathway across mountain ridges, one
425 cross-section across the mountain ridge as shown as one black solid line in Fig. 3 is taken as
426 one example. Figure 10 shows the latitude-height cross section of BC mass concentration and
427 transport flux across one mountain ridge from the simulations with complex and smooth
428 topography at local time (LT) 03:00 and 15:00 averaged for April 1-20, 2016. Near the southern
429 part of mountain, the elevated concentration of BC mass accumulates and can mix up reaching
430 as high as 5 km with the much stronger transport during the daytime. It is obvious that the
431 mountain ridge in the simulation with smooth topography is quite low. With the high mountain
432 ridge resolved by the complex topography, the simulated BC transport flux can still cross the
433 mountain. Analysis of transport flux across a few more mountain ridges indicates similar
434 results (not shown). The results above indicate that the transport of pollutants can cross a

435   majority of mountain ridges of Himalayas, which is consistent with the observation-based

436   estimate by Gong et al. (2019) that also found pollutants could overcome the blocking effect

437   of mountain ridges of Himalayas as a transport pathway. On the other hand, the resolved deeper

438   valleys in the simulation with complex topography enhance the transport flux compared to the

439   one with the smooth topography. Similarly, Figure 11 shows one example of latitude-height

440   cross section of BC mass concentration and transport flux across one valley from the

441   simulations with complex and smooth topography at local time (LT) 03:00 and 15:00 averaged

442   for April 1-20, 2016. The transport is much stronger and deeper along the valley from the

443   simulation with complex topography than the one with smooth topography. Again, analysis of

444   transport flux across a few more valleys does not show different results (not shown).

445   In order to further demonstrate the overall inflow flux across the Himalayas, the vertically

446   integrated BC mass flux along the longitudinal cross section (as shown in Fig. 9) from the

447   simulations with different topography is shown in Figure 12. The terrain heights from the two

448   simulations along the cross section are also shown as black lines. The total mass flux is

449   calculated by integrating the right-hand term of equation (1) as following:

450 $$\mathrm{ITF} = \int_{z=z_{sfc}}^{z=z_{top}} \delta z * C * (u * \sin \alpha + v * \sin \beta) \qquad (2)$$

451   Where δz is the thickness of each vertical model level. Similarly, positive values represent

452   the transport towards the TP, while negative values represent the transport away from the TP.

453   More evidently, the positive BC inflows towards the TP occur not only through the valleys but

454   also across the mountain ridges with both topography. The negative values only exist to the

455   east of 88°E. With complex topography, higher mountain ridges can reduce the transport flux

456   to some extent compared to the smooth topography. The complex topography results in

457   significantly larger BC inflow towards the TP compared to the smooth topography, particularly

458   corresponding to the deep valleys, such as the Karnali River Valley around 82°E and the Kali

459   Gandaki Valley around 84°E.

460   One reason for the enhanced transport across the Himalayas with the complex topography

461   is the resolved deeper valleys that lead to the increased valley wind. The wind across the valleys

462   can be significantly larger with the complex topography than the smooth one (Fig. S4). The

463   enhanced valley wind across the Himalayas has also been found by previous studies with

464   observations and numerical simulations (Egger et al., 2000; Zängl et al., 2001; Carrera et al.,

465   2009; Karki et al., 2017; Lin et al., 2018). The second impact of resolved complex topography

466   on the BC transport is that more BC masses can be transported with the deeper valley channels

467   (Fig. S5a, b). With deeper valley, the column of high-concentration BC is deeper. Even with

468 similar wind velocity, the transport flux can be larger. The third impact is through changing

469 the small-scale circulation around the Himalayas due to the increase of topography complexity

470 of Himalayas. The simulation with complex topography produces more near-surface winds

471 following the direction towards the TP compared to the one with smooth topography (Fig. S6),

472 which favors the BC transport across the Himalayas. Lastly, the simulated PBL heights from

473 the two experiments are a little different (Fig. 9), which may also contribute partly to the

474 different transport flux. The sensitivity of PBL height and structure to topography complexity

475 that can result in different surface heat has been studied before (e.g., Wagner et al., 2014).

476 This turns out that the overall BC inflow with the complex topography is much stronger

477 than that with the smooth topography. Figure 13 shows the accumulated integrated total

478 transport flux of BC across the Himalayas estimated from the simulations with complex and

479 smooth topography for April 1-20, 2016. The accumulated import flux of BC increases during

480 the period in both experiments, and the difference between the two experiments gradually

481 increases with the time. At the end of period, the simulation with complex topography estimates

482 a total import flux of BC of $\sim 1.5 \times 10^4$ Ton that is $\sim 50\%$ higher than $\sim 1.0 \times 10^4$ Ton estimated

483 based on the simulation with smooth topography. The sensitivity analysis by moving the cross

484 line (cross-section of the analysis in Fig. 9, 12, 13) towards or away from the TP within a

485 certain distance and re-calculating the flux indicates that the impacts of topography on the

486 simulated results do not change significantly.

487 All the analysis above focuses on investigating the BC transport flux across the Himalayas.

488 Although the inflow can reflect the impact of transport on the BC mass over the TP to some

489 extent, the change of BC mass concentration is eventually determined by the convergence of

490 transport. Therefore, the contribution of each model process (transport, dry-deposition,

491 emission, PBL mixing, and wet deposition) to the increase of BC column mass averaged over

492 the TP (with elevation > 4 km) during this episode is analyzed for both simulations following

493 the methodology introduced by Du et al. (2020). The results show that the two main processes

494 affecting the BC column mass over the TP during the period are transport and dry deposition.

495 The transport is the dominant process that increases the BC column mass over the TP, while

496 the dry deposition reduces it. The contribution of transport to the increase of BC column mass

497 over the TP during the episode from the simulation with complex topography is significantly

498 larger than that with the smooth topography, which is consistent with the results shown by

499 analyzing the transport flux across the Himalayas.

500

3.3 Radiative forcing of BC over the TP

501

502   The BC transported over the TP could significantly influence the regional climate and

503   water resources over Asia through heating the atmosphere and accelerating the melting of snow

504   and glacier (e.g., Qian et al., 2011, 2015; Lau et al., 2017). Therefore, the impact of the complex

505   topography on estimating the BC radiative heating profile in the atmosphere and radiative

506   forcing in surface snow deserves investigation. Figure 14 shows the vertical profiles of BC

507   induced radiative heating rate in the atmosphere averaged over the TP (with elevation > 4 km)

508   within the inner domain shown in Fig.1 for April 1-20, 2016 from the simulations with complex

509   and smooth topography. Both simulations generate higher BC heating rate near the surface and

510   the rate gradually decreases with altitude, which is consistent with the vertical profiles of BC

511   mass concentration averaged over the TP (Fig. S7 in the supporting material). The BC heating

512   rate over the TP from the simulation with complex topography is ~0.17 K/day near the surface

513   and reduces to ~0.08 K/day at 8 km, which is ~50% and ~30%, respectively, higher than that

514   from the simulation with smooth topography at the corresponding altitudes. The higher BC

515   heating rate over the TP estimated by the simulation with complex topography is consistent

516   with its higher BC column mass (Fig. 5) and concentration profile (Fig. S7).

517   The BC radiative forcing in surface snow is controlled by both the distributions of BC

518   mass concentration and snow coverage (e.g., Zhao et al., 2014). Figure 15 shows the spatial

519   distributions of snow water equivalent (SWE) averaged for April 1-20, 2016 from the

520   simulations with two topography. The difference between the two is also shown. It shows that

521   the simulation with complex topography generates more areas with higher SWE compared to

522   that with the smooth topography over the TP. Along the Himalayas, the simulated SWE is

523   higher over the mountain ridges with the complex topography, particularly for the East

524   Himalayas, while the smooth topography leads to broader snow coverage over the West

525   Himalayas. The difference in SWE between the two simulations is highly correlated with their

526   difference in precipitation (Fig. S8 in the supporting material). Along the Himalayas, the

527   simulated precipitation with the complex topography is larger than that with the smooth

528   topography at the mountain ridges and smaller at the valleys. Over the TP, the overall

529   precipitation is larger with the complex topography than that with the smooth topography (Fig.

530   S8). Previous studies have found that the topography could significantly affect the precipitation

531   over the Himalayas region (e.g., Bookhagen and Burbank, 2010; Wulf et al., 2016; Cannon et

532   al., 2017; Karki et al., 2017).

533   Figure 16 shows the spatial distributions of BC radiative forcing in the surface snow over

534   the TP averaged for April 1-20, 2016 from the simulations with two topography, and the

difference between the two is also shown. The BC radiative forcing in surface snow is largely coincident with the spatial distributions of SWE as shown in Fig. 15, mainly due to the heterogeneous distributions of snow cover over the TP. The BC radiative forcing in surface snow over the TP from the simulation with complex topography reaches 5 W/m^2 where the snow exists, larger than that with the smooth topography. Along the Himalayas, the simulation with complex topography produces higher BC snow forcing over the mountain ridges, particularly over the eastern Himalayas, while the one with the smooth topography simulates higher BC snow forcing over most areas of western Himalayas due to its broader snow coverage there. Overall, the complex topography leads to higher BC forcing in snow over the TP and the eastern Himalayas and lower BC forcing in snow over the western Himalayas, and therefore results in the different distribution of BC forcing in snow over the TP and Himalayas, compared to that with the smooth topography.

4. Summary and discussion

In this study, the model experiments with different topography are conducted to illustrate the impacts of complexity of topography of Himalayas on BC transport from South Asia to the TP. The observed pollution episode at the QOMS station besides the Mt. Everest during the pre-monsoon season is simulated. The observed surface BC concentration shows a peak of ~3 ug/m^3 much larger than the background value of < 0.4 ug/m^3 over the TP. The observed temporal variation of surface BC concentrations correlates highly with that of biomass burning emissions near the southern Himalayas, indicating the significant impacts of biomass burning on the pollutants over the TP. The simulations can reproduce the episode in time and magnitude, and are used to investigate the BC transport mechanisms and the impacts of topography.

The high BC mass loading during the simulation period accumulates near the southern Himalayas driven by the large-scale circulation, which is also observed by satellites. The modeling results demonstrate that the westerly favors the accumulation of pollutants near the southern Himalayas and can carry the pollutants to the TP during the day and night, which is consistent with previous modeling studies (e.g., Kopacz et al., 2011). The transport is stronger across the West Himalayas than that across the East. The deeper PBL during the daytime allows BC over the source region mixed to higher altitude, which also leads to stronger import transport during the day than the night. It is noteworthy that the BC accumulated near the southern Himalayas can be transported across the Himalayas overcoming a majority of mountain ridges, which is consistent with the observation-based estimate by Gong et al. (2019)

568   that also found pollutants could overcome the blocking effect of the mountain ridges of

569   Himalayas. However, the transport through the valleys is found much stronger and more

570   efficient than across the mountain ridges and the enhancement effect cannot be ignored. The

571   complex topography results in 50% higher overall transport flux across the Himalayas during

572   the simulation period than that with the smooth topography, primarily due to the enhanced

573   valley wind, deeper valley channels, and induced small-scale favorable circulation. This turns

574   out that the simulation with complex topography produces 30-50% higher BC radiative heating

575   rate in the atmosphere up to 10 km averaged over the TP than does the simulation with smooth

576   topography.

577   Previous studies also found the induced change of circulation and transport due to the

578   complex topography at convection-permitting scales with the focus on the meteorological

579   fields (e.g., Karki et al., 2017; Lin et al., 2018). However, most of them conducted the sub-10

580   km simulations over a much smaller region (e.g., 101×96 grids at 5 km in Karki et al., 2017,

581   and 181×121 grids at 2 km in Lin et al., 2018) compared to this study (400×300 grids at 4 km).

582   Karki et al. (2017) found that the complex topography resolving more valleys and mountain

583   ridges yielded more realistic strong and narrower winds and also small-scale mountain-valley

584   circulations over the Himalayas region compared to the smoother topography. Lin et al. (2018)

585   analyzed the simulations over the region situated in the central Himalayas (87°E-89°E) with

586   very complex terrain including several high mountains and low valleys, e.g., Mt. Everest, Mt.

587   Kanchenjunga, and the Yadong Valley. Although Lin et al. (2018) simulated enhanced

588   moisture flux along the valley, the overall moisture transported was lower with the complex

589   topography (10 km resolution) compared to that with the smooth topography (30 km

590   resolution). The difference between their study and this study can be due to several factors.

591   First, Lin et al. (2018) focused on a relatively small region of Himalayas (87°E-89°E) compared

592   to that in this study (75°E-92°E). The lower-lever transport flux simulated in this study also

593   exhibits weaker wind with complex topography between 87°E and 89°E (Fig. 9 and 12), maybe

594   due to several very high mountains such as Mt. Everest and Mt. Kanchenjunga over this area.

595   Second, the spatial (horizontal and vertical) distributions between air pollutants and moisture

596   are also different and may contribute partly to the different impacts of topography on the overall

597   transport flux across the Himalayas.

598   For the BC radiative forcing in surface snow, the simulation with complex topography

599   produces stronger forcing over the TP than that with the smooth one. The complex topography

600   makes the distribution of BC forcing in surface snow quite different from the simulation with

601   smooth topography, partly due to its different distribution of surface snow. The simulated BC

602   radiative forcing in snow is distributed more heterogeneously than those in previous studies

603   using global models at relatively coarse resolutions (e.g., Qian et al., 2011). He et al. (2014)

604   used a global chemical transport model to simulate the BC forcing in snow at the horizontal

605   resolution of ~0.2° and obtained the similar distribution as the simulation with smooth

606   topography in this study with the high values over the western Himalayas. However, their

607   simulated values near the Himalayas are higher than the simulated results of this study, which

608   may be due to their estimation are averaged for November-April.

609   This study highlights the importance of resolving complex topography of the Himalayas

610   in modeling the aerosol transport across the Himalayas and radiative impact over the TP.

611   Although this study focuses on the impacts of topography on the simulated results, the

612   additional analysis (Fig. S9-11 in the supporting material) of the outer domain simulation at 20

613   km resolution and the inner domain simulation at 4 km with different topography indicates that

614   the resolution-dependent difference between 20 km and 4 km is largely contributed by their

615   different representations of topography over the Himalayas region, consistent with previous

616   studies (e.g., Karki et al., 2017; Lin et al., 2018). Climate models at coarser horizontal

617   resolutions than 20 km and thus with relatively smooth topography may underestimate the

618   aerosol transport from South Asia to the TP during the pre-monsoon season and represent

619   inappropriately the aerosol radiative forcing in the atmosphere and surface snow over the TP.

620   Since this study only demonstrates the potential impacts for a relatively short period, a longer-

621   term study should be conducted to examine the impacts of topography on aerosol climatic

622   effect over the TP. In addition, the active convection during the monsoon season may also play

623   an important role on pollutant transport across the Himalayas, which deserves further

624   investigation. Furthermore, aerosol impact on cloud and precipitation, particularly during the

625   monsoon season, and thus on the latent heat in the atmosphere and the associated responses

626   may also depend on the complex topography. Previous studies based on observations found

627   that the rain frequency and intensity reached the highest and the cloud thickness reached the

628   deepest at the foothill of Himalayas and decreased as the elevation increased up to the TP (e.g.,

629   Chen et al., 2017; Fu et al., 2018; Zhang et al., 2018), which was explained by Fu et al. (2018)

630   due to the blocking of the air flow by the steep slope of southern Himalayas. However, the

631   large amount of transported aerosol along the slope from the foothill up to the TP may also

632   play a role. These potential impacts of aerosols on regional hydro-climate around the TP and

633   over Asia using high-resolution model that can resolve the complex topography of Himalayas

634   and TP deserve further investigation.

Data availability

The released version of WRF-Chem can be downloaded from http://www2.mmm.ucar.edu/wrf/users/download/get_source.html. The updated USTC version of WRF-Chem can be downloaded from http://aemol.ustc.edu.cn/product/list/ or contact chunzhao@ustc.edu.cn. Also, the code modifications will be incorporated the release version of WRF-Chem in future.

Author contributions

Meixin Zhang and Chun Zhao designed the experiments, conducted and analyzed the simulations. All authors contributed to the discussion and final version of the paper.

Acknowledgements

This research was supported by the National Key Research and Development Program of China (2016YFA0602001), the National Natural Science Foundation of China NSFC (Grant No. 91837310), the second Tibetan Plateau Scientific Expedition and Research Program (STEP) (2019QZKK0605), and the Fundamental Research Funds for the Central Universities. The study used computing resources from the High-Performance Computing Center of University of Science and Technology of China (USTC) and the TH-2 of National Supercomputer Center in Guangzhou (NSCC-GZ).

Reference

Bansal, O., Singh, A., and Singh, D.: Characteristics of Black Carbon aerosols over Patiala Northwestern part of the IGP: Source apportionment using cluster and CWT analysis, Atmospheric Pollution Research, 10, 244–256, doi:10.1016/j.apr.2018.08.001, 2019.

Barnard, J. C., Fast, J. D., Paredes-Miranda, G., Arnott, W. P., and Laskin, A.: Technical Note: Evaluation of the WRF-Chem "Aerosol Chemical to Aerosol Optical Properties" Module using data from the MILAGRO campaign, Atmos. Chem. Phys., 10, 7325–7340, doi:10.5194/acp-10-7325-2010, 2010.

Barnett, T. P., Adam, J. C., and Lettenmaier, D. P.: Potential impacts of a warming climate on water availability in snow-dominated regions, Nature, 438, 303–309, doi:10.1038/nature04141, 2005.

Binkowski, F. S. and Shankar, U.: The Regional Particulate Matter Model: 1. Model description and preliminary results, J. Geophys. Res., 100, 26191, doi:10.1029/95JD02093, 1995.

Bookhagen, B. and Burbank, D. W.: Toward a complete Himalayan hydrological budget: Spatiotemporal distribution of snowmelt and rainfall and their impact on river discharge, J. Geophys. Res., 115, 39, doi:10.1029/2009JF001426, 2010.

Boos, W. R. and Kuang, Z.: Sensitivity of the South Asian monsoon to elevated and non-elevated heating, Scientific reports, 3, 1192, doi:10.1038/srep01192, 2013.

Cannon, F., Carvalho, L. M. V., Jones, C., Norris, J., Bookhagen, B., and Kiladis, G. N.: Effects of topographic smoothing on the simulation of winter precipitation in High Mountain Asia, J. Geophys. Res. Atmos., 122, 1456–1474, doi:10.1002/2016JD026038, 2017.

Cao, J., Tie, X., Xu, B., Zhao, Z., Zhu, C., Li, G., and Liu, S.: Measuring and modeling black carbon (BC) contamination in the SE Tibetan Plateau, Journal of Atmospheric Chemistry, 67, 45-60, doi:10.1007/s10874-011-9202-5, 2010.

Carrera, M. L., Gyakum, J. R., and Lin, C. A.: Observational Study of Wind Channeling within the St. Lawrence River Valley, J. Appl. Meteor. Climatol., 48, 2341–2361, doi:10.1175/2009JAMC2061.1, 2009.

Chapman, E. G., Gustafson, W. I., Easter, R. C., Barnard, J. C., Ghan, S. J., Pekour, M. S., and Fast, J. D.: Coupling aerosol-cloud-radiative processes in the WRF-Chem model: Investigating the radiative impact of elevated point sources, Atmos. Chem. Phys., 9, 945–964, doi:10.5194/acp-9-945-2009, 2009.

691   Chen, J. and Bordoni, S.: Orographic Effects of the Tibetan Plateau on the East Asian Summer

692   Monsoon: An Energetic Perspective, J. Climate, 27, 3052–3072, doi:10.1175/JCLI-D-13-

693   00479.1, 2014.

694   Chen, X., Kang, S., Cong, Z., Yang, J., and Ma, Y.: Concentration, temporal variation, and

695   sources of black carbon in the Mt. Everest region retrieved by real-time observation and

696   simulation, Atmos. Chem. Phys., 18, 12859–12875, doi:10.5194/acp-18-12859-2018, 2018.

697   Chen, X., Kang, S., Cong, Z., Yang, J., and Ma, Y.: Concentration, temporal variation, and

698   sources of black carbon in the Mt. Everest region retrieved by real-time observation and

699   simulation, Atmos. Chem. Phys., 18, 12859–12875, doi:10.5194/acp-18-12859-2018, 2018.

700   Chen, Y., Fu, Y., Xian, T., and Pan, X.: Characteristics of cloud cluster over the steep southern

701   slopes of the Himalayas observed by CloudSat, Int. J. Climatol., 37, 4043–4052,

702   doi:10.1002/joc.4992, 2017.

703   Cong, Z., Kang, S., and Qin, D.: Seasonal features of aerosol particles recorded in snow from

704   Mt. Qomolangma (Everest) and their environmental implications, Journal of environmental

705   sciences (China), 21, 914–919, doi:10.1016/S1001-0742(08)62361-X, 2009.

706   Cong, Z., Kang, S., Kawamura, K., Liu, B., Wan, X., Wang, Z., Gao, S., and Fu, P.:

707   Carbonaceous aerosols on the south edge of the Tibetan Plateau: concentrations, seasonality

708   and sources, Atmos. Chem. Phys., 15, 1573–1584, doi:10.5194/acp-15-1573-2015, 2015a.

709   Cong, Z., Kawamura, K., Kang, S., and Fu, P.: Penetration of biomass-burning emissions from

710   South Asia through the Himalayas: new insights from atmospheric organic acids, Scientific

711   reports, 5, 9580, doi:10.1038/srep09580, 2015b.

712   Dentener, F., Kinne, S., Bond, T., Boucher, O., Cofala, J., Generoso, S., Ginoux, P., Gong, S.,

713   Hoelzemann, J. J., Ito, A., Marelli, L., Penner, J. E., Putaud, J. P., Textor, C., Schulz, M.,

714   van der Werf, G. R., and Wilson, J.: Emissions of primary aerosol and precursor gases in the

715   years 2000 and 1750, prescribed data-sets for AeroCom, Atmos. Chem. Phys., 6, 4321–4344,

716   doi:10.5194/acp-6-4321-2006, 2006.

717   Ding, Y., Sun, Y., Wang, Z., Zhu, Y., and Song, Y.: Inter-decadal variation of the summer

718   precipitation in China and its association with decreasing Asian summer monsoon Part II:

719   Possible causes, Int. J. Climatol., 29, 1926–1944, doi:10.1002/joc.1759, 2009.

720   Du, Q., Zhao, C., Zhang, M., Dong, X., Chen, Y., Liu, Z., Hu, Z., Zhang, Q., Li, Y., Yuan, R.

721   , and Miao, S.: Modelling diurnal variation of surface PM2.5 concentration over East China

722   with WRF-Chem: Impacts from boundary layer mixing and anthropogenic

723   emission, Atmos. Chem. Phys. Discuss., https://doi.org/10.5194/acp-2019-

724   739, in review, 2020.

725 Duan, A. M. and Wu, G. X.: Role of the Tibetan Plateau thermal forcing in the summer climate

726 patterns over subtropical Asia, Climate Dynamics, 24, 793–807, doi:10.1007/s00382-004-

727 0488-8, 2005.

728 Dubovik, O. and King, M. D.: A flexible inversion algorithm for retrieval of aerosol optical

729 properties from Sun and sky radiance measurements, J. Geophys. Res., 105, 20673–20696,

730 doi:10.1029/2000JD900282, 2000.

731 Dubovik, O., Holben, B., Eck, T. F., Smirnov, A., Kaufman, Y. J., King, M. D., Tanré, D., and

732 Slutsker, I.: Variability of Absorption and Optical Properties of Key Aerosol Types

733 Observed in Worldwide Locations, J. Atmos. Sci., 59, 590–608, doi:10.1175/1520-

734 0469(2002)059<0590:VOAAOP>2.0.CO;2, 2002.

735 Dumka, U. C., Moorthy, K. K., Kumar, R., Hegde, P., Sagar, R., Pant, P., Singh, N., and Babu,

736 S. S.: Characteristics of aerosol black carbon mass concentration over a high altitude location

737 in the Central Himalayas from multi-year measurements, Atmospheric Research, 96, 510–

738 521, doi:10.1016/j.atmosres.2009.12.010, 2010.

739 Easter, R. C., Ghan, S. J., Zhang, Y., Saylor, R. D., Chapman, E. G., Laulainen, N. S., Abdul-

740 Razzak, H., Leung, L. R., Bian, X., and Zaveri, R. A.: MIRAGE: Model Description and

741 Evaluation of Aerosols and Trace Gases, J. Geophys. Res., 109, D20210,

742 doi:10.1029/2004JD004571, 2004.

743 Egger, J., Bajracharya, S., Egger, U., Heinrich, R., Reuder, J., Shakya, P., Wendt, H., and Wirth,

744 V.: Diurnal winds in the Himalayan Kali Gandaki Valley. Part I: Observations, Mon.

745 Weather Rev., 128, 1106–1122, 2000.

746 Engling, G. and Gelencser, A.: Atmospheric Brown Clouds: From Local Air Pollution to

747 Climate Change, Elements, 6, 223–228, doi:10.2113/gselements.6.4.223, 2010.

748 Fan, J., Rosenfeld, D., Yang, Y., Zhao, C., Leung, L. R., and Li, Z.: Substantial contribution

749 of anthropogenic air pollution to catastrophic floods in Southwest China, Geophys. Res. Lett.,

750 42, 6066–6075, doi:10.1002/2015GL064479, 2015.

751 Fast, J. D., Gustafson Jr, W. I., Easter, R. C., Zaveri, R. A., Barnard, J. C., Chapman, E. G.,

752 Grell, G. A., and Peckham, S. E.: Evolution of ozone, particulates, and aerosol direct

753 radiative forcing in the vicinity of Houston using a fully coupled meteorology-chemistry-

754 aerosol model, J. Geophys. Res., 111, D21305, doi:10.1029/2005JD006721, 2006.

755 Feng, Y., Kotamarthi, V. R., Coulter, R., Zhao, C., and Cadeddu, M.: Radiative and

756 thermodynamic responses to aerosol extinction profiles during the pre-monsoon month over

757 South Asia, Atmos. Chem. Phys., 16, 247–264, doi:10.5194/acp-16-247-2016, 2016.

758 Flanner, M. G. and Zender, C. S.: Snowpack radiative heating: Influence on Tibetan Plateau
759   climate, Geophys. Res. Lett., 32, L06501, doi:10.1029/2004GL022076, 2005.

760 Fu, Y., Pan, X., Xian, T., Liu, G., Zhong, L., Liu, Q., Li, R., Wang, Y., and Ma, M.:
761   Precipitation characteristics over the steep slope of the Himalayas in rainy season observed
762   by TRMM PR and VIRS, Climate dynamics, 51, 1971-1989, doi: 10.1007/s00382-017-
763   3992-3, 2018.

764 Gao, Y., Zhao, C., Liu, X., Zhang, M., and Leung, L. R.: WRF-Chem simulations of aerosols
765   and anthropogenic aerosol radiative forcing in East Asia, Atmospheric Environment, 92,
766   250–266, doi:10.1016/j.atmosenv.2014.04.038, 2014.

767 Ginoux, P., Chin, M., Tegen, I., Prospero, J. M., Holben, B., Dubovik, O., and Lin, S.-J.:
768   Sources and distributions of dust aerosols simulated with the GOCART model, J. Geophys.
769   Res., 106, 20255–20273, doi:10.1029/2000JD000053, 2001.

770 Gong, P., Wang, X., Pokhrel, B., Wang, H., Liu, X., Liu, X., and Wania, F.: Trans-Himalayan
771   Transport of Organochlorine Compounds: Three-Year Observations and Model-Based Flux
772   Estimation, Environ. Sci. Technol., 53, 6773–6783, doi:10.1021/acs.est.9b01223, 2019.

773 Gong, S. L.: A parameterization of sea-salt aerosol source function for sub- and super-micron
774   particles, Global Biogeochem. Cycles, 17, n/a-n/a, doi:10.1029/2003GB002079, 2003.

775 Grell, G. A., Peckham, S. E., Schmitz, R., McKeen, S. A., Frost, G., Skamarock, W. C., and
776   Eder, B.: Fully coupled "online" chemistry within the WRF model, Atmospheric
777   Environment, 39, 6957–6975, doi:10.1016/j.atmosenv.2005.04.027, 2005.

778 Gustafson, W. I., E. G. Chapman, S. J. Ghan, R. C. Easter, and J. D. Fast: Impact on modeled
779   cloud characteristics due to simplified treatment of uniform cloud condensation nuclei
780   during NEAQS 2004, Geophys. Res. Lett., 34, L19809, doi:10.1029/2007GL030021, 2007.

781 Hansen, J. and Nazarenko, L.: Soot climate forcing via snow and ice albedos, Proceedings of
782   the National Academy of Sciences, 101, 423–428, doi:10.1073/pnas.2237157100, 2004.

783 He, C., Li, Q., Liou, K. N., Takano, Y., Gu, Y., Qi, L., Mao, Y., and Leung, L. R.: Black carbon
784   radiative forcing over the Tibetan Plateau, Geophys. Res. Lett., 41, 7806–7813,
785   doi:10.1002/2014GL062191, 2014.

786 He, C., Wang, Z., Zhou, T., and Li, T.: Enhanced Latent Heating over the Tibetan Plateau as a
787   Key to the Enhanced East Asian Summer Monsoon Circulation under a Warming Climate,
788   J. Climate, 32, 3373–3388, doi:10.1175/JCLI-D-18-0427.1, 2019.

789 Hess, M., Koepke, P., and Schult, I.: Optical Properties of Aerosols and Clouds: The Software
790   Package OPAC, Bull. Amer. Meteor. Soc., 79, 831–844, doi:10.1175/1520-
791   0477(1998)079<0831:OPOAAC>2.0.CO;2, 1998.

Hindman, E. E. and Upadhyay, B. P.: Air pollution transport in the Himalayas of Nepal and Tibet during the 1995–1996 dry season, Atmospheric Environment, 36, 727–739, doi:10.1016/S1352-2310(01)00495-2, 2002.

Holben, B. N., Eck, T. F., Slutsker, I., Tanré, D., Buis, J. P., Setzer, A., Vermote, E., Reagan, J. A., Kaufman, Y. J., Nakajima, T., Lavenu, F., Jankowiak, I., and Smirnov, A.: AERONET—A Federated Instrument Network and Data Archive for Aerosol Characterization, Remote Sensing of Environment, 66, 1–16, doi:10.1016/S0034-4257(98)00031-5, 1998.

Holben, B. N., Tanre, D., Smirnov, A., ECK T. F., Slutsker, I., Abuhassan, N., Newcomb, W., Schafer, J., Chatenet, B., Lavenu, F., Kaufman, Y., Vande Castle, J., Setzer, A., Markham, B., Clark, D., Frouin, R., Halthore, R., Karneli, A., O'Neill, N., Pietras, C., Pinker, R., Voss, K., and Zibordi, G.: An emerging ground-based aerosol climatology: Aerosol optical depth from AERONET, J. Geophys. Res., 106, 12067-12097, doi:10.1029/2001JD900014, 2001.

Hu, Z., Huang, J., Zhao, C., Bi, J., Jin, Q., Qian, Y., Leung, L. R., Feng, T., Chen, S., and Ma, J.: Modeling the contributions of Northern Hemisphere dust sources to dust outflow from East Asia, Atmospheric Environment, 202, 234–243, doi:10.1016/j.atmosenv.2019.01.022, 2019.

Hu, Z., Huang, J., Zhao, C., Jin, Q., Ma, Y., and Yang, B.: Modeling dust sources, transport, and radiative effects at different altitudes over the Tibetan Plateau, Atmos. Chem. Phys. Discuss., https://doi.org/10.5194/acp-2019-431, in press, 2020.

Hu, Z., Zhao, C., Huang, J., Leung, L. R., Qian, Y., Yu, H., Huang, L., and Kalashnikova, O.V.: Trans-pacific transport and evolution of aerosols: Evaluation of quasi global WRF-Chem simulation with multiple observations, Geosci. Model Dev. Discuss., 1–65, doi:10.5194/gmd-2015-248, 2016.

Huang, X., Song, Y., Zhao, C., Cai, X., Zhang, H., and Zhu, T.: Direct Radiative Effect by Multicomponent Aerosol over China, J. Climate, 28, 3472–3495, doi:10.1175/JCLI-D-14-00365.1, 2015.

Iacono, M. J., Mlawer, E. J., Clough, S. A., and Morcrette, J. J.: Impact of an improved longwave radiation model, RRTM, on the energy budget and thermodynamic properties of the NCAR community climate model, CCM3, J. Geophys. Res., 105, 14873–14890, doi:10.1029/2000JD900091, 2000.

Immerzeel, W. W., van Beek, L. P. H., and Bierkens, M. F. P.: Climate change will affect the Asian water towers, Science (New York, N.Y.), 328, 1382–1385, doi:10.1126/science.1183188, 2010.

828 Jaeglé, L., Quinn, P. K., Bates, T. S., Alexander, B., and Lin, J. T.: Global distribution of sea
829   salt aerosols: new constraints from in situ and remote sensing observations, Atmos. Chem.
830   Phys., 11, 3137–3157, doi:10.5194/acp-11-3137-2011, 2011.

831 Janssens-Maenhout, G., Crippa, M., Guizzardi, D., Dentener, F., Muntean, M., Pouliot, G.,
832   Keating, T., Zhang, Q., Kurokawa, J., Wankmüller, R., van der Denier Gon, H., Kuenen, J.
833   J. P., Klimont, Z., Frost, G., Darras, S., Koffi, B., and Li, M.: HTAP_v2.2: a mosaic of
834   regional and global emission grid maps for 2008 and 2010 to study hemispheric transport of
835   air pollution, Atmos. Chem. Phys., 15, 11411–11432, doi:10.5194/acp-15-11411-2015,
836   2015.

837 Ji, Z. M.: Modeling black carbon and its potential radiative effects over the Tibetan Plateau,
838   Advances in Climate Change Research, 7, 139–144, doi:10.1016/j.accre.2016.10.002, 2016.

839 Ji, Z., Kang, S., Cong, Z., Zhang, Q., and Yao, T.: Simulation of carbonaceous aerosols over
840   the Third Pole and adjacent regions: distribution, transportation, deposition, and climatic
841   effects, Clim Dyn, 45, 2831–2846, doi:10.1007/s00382-015-2509-1, 2015.

842 Kain, J. S.: The Kain–Fritsch Convective Parameterization: An Update, J. Appl. Meteor., 43,
843   170–181, doi:10.1175/1520-0450(2004)043<0170:TKCPAU>2.0.CO;2, 2004.

844 Kang, S., Q. Zhang, Y. Qian, Z. Ji, C. Li, Z. Cong, Y. Zhang, J. Guo, W. Du, J. Huang, Q. You,
845   A. K. Panday, M. Rupakheti, D. Chen, O. Gustafsson, M. H. Thiemens, and D. Qin: Linking
846   atmospheric pollution to cryospheric change in the Third Pole region: current progress and
847   future prospects, National Science Review, 6, 796–809, doi:10.1093/nsr/nwz031, 2019.

848 Kang, S.: Atmospheric Aerosol Elements over the Inland Tibetan Plateau: Concentration,
849   Seasonality, and Transport, Aerosol Air Qual. Res., doi:10.4209/aaqr.2015.02.0307, 2015.

850 Kant, Y., Shaik, D. S., Mitra, D., Chandola, H. C., Babu, S. S., and Chauhan, P.: Black carbon
851   aerosol quantification over north-west Himalayas: Seasonal heterogeneity, source
852   apportionment and radiative forcing, Environmental pollution (Barking, Essex 1987),
853   113446, doi:10.1016/j.envpol.2019.113446, 2019.

854 Karki, R., ul Hasson, S., Gerlitz, L., Schickhoff, U., Scholten, T., and Böhner, J.: Quantifying
855   the added value of convection-permitting climate simulations in complex terrain: a
856   systematic evaluation of WRF over the Himalayas, Earth Syst. Dynam., 8, 507–528,
857   doi:10.5194/esd-8-507-2017, 2017.

858 Kok, J. F.: A scaling theory for the size distribution of emitted dust aerosols suggests climate
859   models underestimate the size of the global dust cycle, Proceedings of the National Academy
860   of Sciences of the United States of America, 108, 1016–1021, doi:10.1073/pnas.1014798108,
861   2011.

Kopacz, M., Mauzerall, D. L., Wang, J., Leibensperger, E. M., Henze, D. K., and Singh, K.: Origin and radiative forcing of black carbon transported to the Himalayas and Tibetan Plateau, Atmos. Chem. Phys., 11, 2837–2852, doi:10.5194/acp-11-2837-2011, 2011.

Kuhlmann, J. and Quaas, J.: How can aerosols affect the Asian summer monsoon? Assessment during three consecutive pre-monsoon seasons from CALIPSO satellite data, Atmos. Chem. Phys., 10, 4673–4688, doi:10.5194/acp-10-4673-2010, 2010.

Lau, K. M. and Kim, K. M.: Observational relationships between aerosol and Asian monsoon rainfall, and circulation, Geophys. Res. Lett., 33, D22101, doi: 10.1029/2006GL027546, 2006b.

Lau, K. M., Kim, M. K., and Kim, K. M.: Asian summer monsoon anomalies induced by aerosol direct forcing: the role of the Tibetan Plateau, Clim Dyn, 26, 855–864, doi: 10.1007/s00382-006-0114-z, 2006a.

Lau, W. K. and Kim, K. M.: Impact of Snow Darkening by Deposition of Light-Absorbing Aerosols on Snow Cover in the Himalayas–Tibetan Plateau and Influence on the Asian Summer Monsoon: A Possible Mechanism for the Blanford Hypothesis, Atmosphere, 9, 438, doi:10.3390/atmos9110438, 2018.

Lau, W. K. M., Kim, K. M., Shi, J. J., Matsui, T., Chin, M., Tan, Q., Peters-Lidard, C., and Tao, W. K.: Impacts of aerosol–monsoon interaction on rainfall and circulation over Northern India and the Himalaya Foothills, Clim Dyn, 49, 1945–1960, doi:10.1007/s00382-016-3430-y, 2017.

Lau, W. K. M., Kim, M. K., Kim, K. M., and Lee, W. S.: Enhanced surface warming and accelerated snow melt in the Himalayas and Tibetan Plateau induced by absorbing aerosols, Environ. Res. Lett., 5, 25204, doi:10.1088/1748-9326/5/2/025204, 2010.

Lee, W. S., Bhawar, R. L., Kim, M. K., and Sang, J.: Study of aerosol effect on accelerated snow melting over the Tibetan Plateau during boreal spring, Atmospheric Environment, 75, 113–122, doi:10.1016/j.atmosenv.2013.04.004, 2013.

Li, C., Bosch, C., Kang, S., Andersson, A., Chen, P., Zhang, Q., Cong, Z., Chen, B., Qin, D., and Gustafsson, Ö.: Sources of black carbon to the Himalayan–Tibetan Plateau glaciers, Nat Commun, 7, 4825, doi:10.1038/ncomms12574, 2016.

Li, M., Zhang, Q., Kurokawa, J. i., Woo, J. H., He, K., Lu, Z., Ohara, T., Song, Y., Streets, D. G., Carmichael, G. R., Cheng, Y., Hong, C., Huo, H., Jiang, X., Kang, S., Liu, F., Su, H., and Zheng, B.: MIX: a mosaic Asian anthropogenic emission inventory under the international collaboration framework of the MICS-Asia and HTAP, Atmos. Chem. Phys., 17, 935–963, doi:10.5194/acp-17-935-2017, 2017.

896 Li, R. and Min, Q. L.: Impacts of mineral dust on the vertical structure of precipitation, J.
897   Geophys. Res., 115, 1337, doi:10.1029/2009JD011925, 2010.

898 Li, R., Dong, X., Guo, J., Fu, Y., Zhao, C., Wang, Y., and Min, Q.: The implications of dust
899   ice nuclei effect on cloud top temperature in a complex mesoscale convective system, Sci
900   Rep, 7, 291, doi:10.1038/s41598-017-12681-0, 2017.

901 Li, R., Shao, W., Guo, J., Fu, Y., Wang, Y., Liu, G., Zhou, R., and Li, W.: A Simplified
902   Algorithm to Estimate Latent Heating Rate Using Vertical Rainfall Profiles Over the Tibetan
903   Plateau, J. Geophys. Res. Atmos., 124, 942–963, doi:10.1029/2018JD029297, 2019.

904 Lin, C., Chen, D., Yang, K., and Ou, T.: Impact of model resolution on simulating the water
905   vapor transport through the central Himalayas: implication for models' wet bias over the
906   Tibetan Plateau, Clim Dyn, 51, 3195–3207, doi:10.1007/s00382-018-4074-x, 2018.

907 Liu, P., Tsimpidi, A. P., Hu, Y., Stone, B., Russell, A. G., and Nenes, A.: Differences between
908   downscaling with spectral and grid nudging using WRF, Atmos. Chem. Phys., 12, 3601–
909   3610, doi:10.5194/acp-12-3601-2012, 2012.

910 Liu, Y., Sato, Y., Jia, R., Xie, Y., Huang, J., and Nakajima, T.: Modeling study on the transport
911   of summer dust and anthropogenic aerosols over the Tibetan Plateau, Atmos. Chem. Phys.,
912   15, 12581–12594, doi:10.5194/acp-15-12581-2015, 2015.

913 Liu, Z., Ming, Y., Zhao, C., Lau, N. C., Guo, J., Bollasina, M., and Yim, S. H. L.: Contribution
914   of local and remote anthropogenic aerosols to a record-breaking torrential rainfall event in
915   Guangdong Province, China, Atmos. Chem. Phys., 20, 223–241, doi:10.5194/acp-20-223-
916   2020, 2020.

917 Lu, Z., Streets, D. G., Zhang, Q., and Wang, S.: A novel back-trajectory analysis of the origin
918   of black carbon transported to the Himalayas and Tibetan Plateau during 1996-2010,
919   Geophys. Res. Lett., 39, n/a-n/a, doi:10.1029/2011GL049903, 2012.

920 Lüthi, Z. L., Škerlak, B., Kim, S. W., Lauer, A., Mues, A., Rupakheti, M., and Kang, S.:
921   Atmospheric brown clouds reach the Tibetan Plateau by crossing the Himalayas, Atmos.
922   Chem. Phys., 15, 6007–6021, doi:10.5194/acp-15-6007-2015, 2015.

923 Lutz, A. F., Immerzeel, W. W., Shrestha, A. B., and Bierkens, M. F. P.: Consistent increase in
924   High Asia's runoff due to increasing glacier melt and precipitation, Nature Clim Change, 4,
925   587–592, doi:10.1038/nclimate2237, 2014.

926 Marinoni, A., Cristofanelli, P., Laj, P., Duchi, R., Calzolari, F., Decesari, S., Sellegri, K.,
927   Vuillermoz, E., Verza, G. P., and Villani, P.: Aerosol mass and black carbon concentrations,
928   a two year record at NCO-P (5079 m, Southern Himalayas), Atmos. Chem. Phys., 10, 8551–
929   8562, doi:10.5194/acp-10-8551-2010, 2010.

930 Menon, S., Koch, D., Beig, G., Sahu, S., Fasullo, J., and Orlikowski, D.: Black carbon aerosols
931   and the third polar ice cap, Atmos. Chem. Phys., 10, 4559–4571, doi:10.5194/acp-10-4559-
932   2010, 2010.

933 Ming, J., Xiao, C., Cachier, H., Qin, D., Qin, X., Li, Z., and Pu, J.: Black Carbon (BC) in the
934   snow of glaciers in west China and its potential effects on albedos, Atmospheric Research,
935   92, 114–123, doi:10.1016/j.atmosres.2008.09.007, 2009.

936 Mlawer, E. J., Taubman, S. J., Brown, P. D., Iacono, M. J., and Clough, S. A.: Radiative
937   transfer for inhomogeneous atmospheres: RRTM, a validated correlated-k model for the
938   longwave, J. Geophys. Res., 102, 16663–16682, doi:10.1029/97JD00237, 1997.

939 Morrison, H., Thompson, G., and Tatarskii, V.: Impact of Cloud Microphysics on the
940   Development of Trailing Stratiform Precipitation in a Simulated Squall Line: Comparison
941   of One- and Two-Moment Schemes, Mon. Wea. Rev., 137, 991–1007,
942   doi:10.1175/2008MWR2556.1, 2009.

943 Nakanishi, M. and Niino, H.: An Improved Mellor–Yamada Level-3 Model: Its Numerical
944   Stability and Application to a Regional Prediction of Advection Fog, Boundary-Layer
945   Meteorol, 119, 397–407, doi:10.1007/s10546-005-9030-8, 2006.

946 Oleson, K. W., Lawrence, D. M., Bonan, G. B., Flanner, M. G., Kluzek, E., Lawrence, P. J.,
947   Levis, S., Swenson, S. C., Thornton, P. E., Dai, A., Decker, M., Dickinson, R., Feddema, J.,
948   Heald, C. L., Hoffman, F., Lamarque, J. F., Mahowald, N., Niu, G. Y., Qian, T., Randerson,
949   J., Running, S., Sakaguchi, K., Slater, A., Stockli, R., Wang, A., Yang, Z. L., Zeng, X., and
950   Zeng, X.: Technical Description of version 4.0 of the Community Land Model (CLM), Tech.
951   Rep. NCAR/TN-478+STR, National Center for Atmospheric Research, Boulder, Colorado,
952   USA, 2010.

953 Prasad, A. K. and Singh, R. P.: Comparison of MISR-MODIS aerosol optical depth over the
954   Indo-Gangetic basin during the winter and summer seasons (2000–2005), Remote Sensing
955   of Environment, 107, 109–119, doi:10.1016/j.rse.2006.09.026, 2007.

956 Qian, Y., Flanner, M. G., Leung, L. R., and Wang, W.: Sensitivity studies on the impacts of
957   Tibetan Plateau snowpack pollution on the Asian hydrological cycle and monsoon climate,
958   Atmos. Chem. Phys., 11, 1929–1948, doi:10.5194/acp-11-1929-2011, 2011.

959 Qian, Y., Yasunari, T. J., Doherty, S. J., Flanner, M. G., Lau, W. K. M., Ming, J., Wang, H.,
960   Wang, M., Warren, S. G., and Zhang, R.: Light-absorbing particles in snow and ice:
961   Measurement and modeling of climatic and hydrological impact, Adv. Atmos. Sci., 32, 64–
962   91, doi:10.1007/s00376-014-0010-0, 2015.

963 Qiu, J.: China: The third pole, Nature, 454, 393–396, doi:10.1038/454393a, 2008.

964   Ramanathan, V. and Carmichael, G.: Global and regional climate changes due to black carbon,
965   Nature Geosci, 1, 221–227, doi:10.1038/ngeo156, 2008.

966   Ramanathan, V., Ramana, M. V., Roberts, G., Kim, D., Corrigan, C., Chung, C., and Winker,
967   D.: Warming trends in Asia amplified by brown cloud solar absorption, Nature, 448, 575–
968   578, doi:10.1038/nature06019, 2007.

969   Sarangi, C., Qian, Y., Rittger, K., Bormann, K. J., Liu, Y., Wang, H., Lin, G., and Painter, T.
970   H.: Impact of light-absorbing particles on snow albedo darkening and associated radiative
971   forcing over high-mountain Asia: high-resolution WRF-Chem modeling and new satellite
972   observations. Atmos. Chem. Phys., 19, 7105–7128, doi:10.5194/acp-19-7105-2019, 2019.

973   Seaman, N. L., Stauffer, D. R., and Lario-Gibbs, A. M.: A Multiscale Four-Dimensional Data
974   Assimilation System Applied in the San Joaquin Valley during SARMAP. Part I: Modeling
975   Design and Basic Performance Characteristics, J. Appl. Meteor., 34, 1739–1761,
976   doi:10.1175/1520-0450(1995)034<1739:AMFDDA>2.0.CO;2, 1995.

977   Shi, X., Wang, Y., and Xu, X.: Effect of mesoscale topography over the Tibetan Plateau on
978   summer precipitation in China: A regional model study, Geophys. Res. Lett., 35, 255,
979   doi:10.1029/2008GL034740, 2008.

980   Singh, P. and Bengtsson, L.: Hydrological sensitivity of a large Himalayan basin to climate
981   change, Hydrol. Process., 18, 2363–2385, doi:10.1002/hyp.1468, 2004.

982   Skamarock, W. C., Klemp, J. B., Dudhia, J., Gill, D. O., Barker, D. M., Duda, M., Huang, X.
983   Y., Wang, W., and Powers, J. G.: A Description of the Advanced Research WRF Version 3,
984   NCAR Technical Note, NCAR/TN-468+STR, available at: http://wrf-
985   model.org/wrfadmin/docs/arw v2.pdf, 2008.

986   Stauffer, D. R. and Seaman, N. L.: Use of Four-Dimensional Data Assimilation in a Limited-
987   Area Mesoscale Model. Part I: Experiments with Synoptic-Scale Data, Mon. Wea. Rev., 118,
988   1250–1277, doi:10.1175/1520-0493(1990)118<1250:UOFDDA>2.0.CO;2, 1990.

989   Wagner, J. S., Gohm, A., and Rotach, M. W.: The Impact of Horizontal Model Grid Resolution
990   on the Boundary Layer Structure over an Idealized Valley, Mon. Wea. Rev., 142, 3446–
991   3465, doi:10.1175/MWR-D-14-00002.1, 2014.

992   Wang, X., Gong, P., Sheng, J., Joswiak, D. R., and Yao, T.: Long-range atmospheric transport
993   of particulate Polycyclic Aromatic Hydrocarbons and the incursion of aerosols to the
994   southeast Tibetan Plateau, Atmospheric Environment, 115, 124–131,
995   doi:10.1016/j.atmosenv.2015.04.050, 2015.

996   Wiedinmyer, C., Akagi, S. K., Yokelson, R. J., Emmons, L. K., Al-Saadi, J. A., Orlando, J. J.,
997   and Soja, A. J.: The Fire INventory from NCAR (FINN): a high resolution global model to

998   estimate the emissions from open burning, Geosci. Model Dev., 4, 625–641,
999   doi:10.5194/gmd-4-625-2011, 2011.

1000 Wu, G., Liu, Y., Dong, B., Liang, X., Duan, A., Bao, Q., and Yu, J.: Revisiting Asian monsoon
1001   formation and change associated with Tibetan Plateau forcing: I. Formation, Clim Dyn, 39,
1002   1169–1181, doi:10.1007/s00382-012-1334-z, 2012.

1003 Wu, G., Liu, Y., He, B., Bao, Q., Duan, A., and Jin, F.-F.: Thermal controls on the Asian
1004   summer monsoon, Scientific reports, 2, 404, doi:10.1038/srep00404, 2012.

1005 Wu, G., Liu, Y., Zhang, Q., Duan, A., Wang, T., Wan, R., Liu, X., Li, W., Wang, Z., and Liang,
1006   X.: The Influence of Mechanical and Thermal Forcing by the Tibetan Plateau on Asian
1007   Climate, J. Hydrometeor., 8, 770–789, doi:10.1175/JHM609.1, 2007.

1008 Wu, L., Su, H., and Jiang, J. H.: Regional simulation of aerosol impacts on precipitation during
1009   the East Asian summer monsoon, J. Geophys. Res. Atmos., 118, 6454–6467,
1010   doi:10.1002/jgrd.50527, 2013.

1011 Wulf, H., Bookhagen, B., and Scherler, D.: Differentiating between rain, snow, and glacier
1012   contributions to river discharge in the western Himalaya using remote-sensing data and
1013   distributed hydrological modeling, Advances in Water Resources, 88, 152–169,
1014   doi:10.1016/j.advwatres.2015.12.004, 2016.

1015 Yang, J., Kang, S., Ji, Z., and Chen, D.: Modeling the Origin of Anthropogenic Black Carbon
1016   and Its Climatic Effect Over the Tibetan Plateau and Surrounding Regions, J. Geophys. Res.
1017   Atmos., 123, 671–692, doi:10.1002/2017JD027282, 2018.

1018 Yasunari, T. J., Bonasoni, P., Laj, P., Fujita, K., Vuillermoz, E., Marinoni, A., Cristofanelli, P.,
1019   Duchi, R., Tartari, G., and Lau, K.-M.: Estimated impact of black carbon deposition during
1020   pre-monsoon season from Nepal Climate Observatory – Pyramid data and snow albedo
1021   changes over Himalayan glaciers, Atmos. Chem. Phys., 10, 6603–6615, doi:10.5194/acp-
1022   10-6603-2010, 2010.

1023 Ye, D. Z. and Wu, G. X.: The role of the heat source of the Tibetan Plateau in the general
1024   circulation, Meteorl. Atmos. Phys., 67, 181–198, doi:10.1007/BF01277509, 1998.

1025 Zängl, G., Egger, J., and Wirth, V.: Diurnal Winds in the Himalayan Kali Gandaki Valley. Part
1026   II: Modeling, Mon. Wea. Rev., 129, 1062–1080, doi:10.1175/1520-
1027   0493(2001)129<1062:DWITHK>2.0.CO;2, 2001.

1028 Zaveri, R. A. and Peters, L. K.: A new lumped structure photochemical mechanism for large-
1029   scale applications, J. Geophys. Res., 104, 30387–30415, doi:10.1029/1999JD900876, 1999.

1030   Zaveri, R. A., Easter, R. C., Fast, J. D., and Peters, L. K.: Model for Simulating Aerosol

1031   Interactions and Chemistry (MOSAIC), J. Geophys. Res., 113, 1591,

1032   doi:10.1029/2007JD008782, 2008.

1033   Zhang, A., Fu, Y., Chen, Y., Liu, G., and Zhang, X.: Impact of the surface wind flow on

1034   precipitation characteristics over the southern Himalayas: GPM observations, Atmospheric

1035   Research, 202, 10–22, doi:10.1016/j.atmosres.2017.11.001, 2018.

1036   Zhang, R., Wang, H., Qian, Y., Rasch, P. J., Easter, R. C., Ma, P. L., Singh, B., Huang, J., and

1037   Fu, Q.: Quantifying sources, transport, deposition, and radiative forcing of black carbon over

1038   the Himalayas and Tibetan Plateau, Atmos. Chem. Phys., 15, 6205–6223, doi:10.5194/acp-

1039   15-6205-2015, 2015.

1040   Zhang, R., Wang, Y., He, Q., Chen, L., Zhang, Y., Qu, H., Smeltzer, C., Li, J., Alvarado, L. M.

1041   A., Vrekoussis, M., Richter, A., Wittrock, F., and Burrows, J. P.: Enhanced trans-Himalaya

1042   pollution transport to the Tibetan Plateau by cut-off low systems, Atmos. Chem. Phys., 17,

1043   3083–3095, doi:10.5194/acp-17-3083-2017, 2017.

1044   Zhang, Y., Kang, S., Cong, Z., Schmale, J., Sprenger, M., Li, C., Yang, W., Gao, T., Sillanpää,

1045   M., Li, X., Liu, Y., Chen, P., and Zhang, X.: Light-absorbing impurities enhance glacier

1046   albedo reduction in the southeastern Tibetan plateau, J. Geophys. Res. Atmos., 122, 6915–

1047   6933, doi:10.1002/2016JD026397, 2017.

1048   Zhang, Y., Kang, S., Sprenger, M., Cong, Z., Gao, T., Li, C., Tao, S., Li, X., Zhong, X., Xu,

1049   M., Meng, W., Neupane, B., Qin, X., and Sillanpää, M.: Black carbon and mineral dust in

1050   snow cover on the Tibetan Plateau, The Cryosphere, 12, 413–431, doi:10.5194/tc-12-413-

1051   2018, 2018.

1052   Zhao, C., Chen, S., Leung, L. R., Qian, Y., Kok, J., Zaveri, R., and Huang, J.: Uncertainty in

1053   modeling dust mass balance and radiative forcing from size parameterization, Atmos. Chem.

1054   Phys., 13, 10733–10753, doi:doi:10.5194/acp-13-10733-2013, 2013b.

1055   Zhao, C., Hu, Z., Qian, Y., Leung, L. R., Huang, J., Huang, M., Jin, J., Flanner, M., Zhang, R.,

1056   Wang, H., Yan, H., Lu, Z., and Streets, D. G.: Simulating black carbon and dust and their

1057   radiative forcing in seasonal snow: a case study over North China with field campaign

1058   measurements, Atmos. Chem. Phys., 14, 11475–11491, doi:10.5194/acp-14-11475-2014,

1059   2014.

1060   Zhao, C., Huang, M., Fast, J. D., Berg, L. K., Qian, Y., Guenther, A., Gu, D., Shrivastava, M.,

1061   Liu, Y., and Walters, S.: Sensitivity of biogenic volatile organic compounds to land surface

1062   parameterizations and vegetation distributions in California, Geosci. Model Dev, 9, 1959–

1063   1976, doi:10.5194/gmd-9-1959-2016, 2016.

1064 Zhao, C., Liu, X., and Leung, L. R.: Impact of the Desert dust on the summer monsoon system
1065   over Southwestern North America, Atmos. Chem. Phys., 12, 3717–3731, doi:10.5194/acp-
1066   12-3717-2012, 2012.

1067 Zhao, C., Liu, X., Leung, L. R., and Hagos, S.: Radiative impact of mineral dust on monsoon
1068   precipitation variability over West Africa, Atmos. Chem. Phys., 11, 1879–1893,
1069   doi:10.5194/acp-11-1879-2011, 2011.

1070 Zhao, C., Liu, X., Leung, L. R., Johnson, B., McFarlane, S. A., Gustafson, W. I., Fast, J. D.,
1071   and Easter, R.: The spatial distribution of mineral dust and its shortwave radiative forcing
1072   over North Africa: modeling sensitivities to dust emissions and aerosol size treatments,
1073   Atmos. Chem. Phys., 10, 8821–8838, doi:10.5194/acp-10-8821-2010, 2010.

1074 Zhao, C., Ruby Leung, L., Easter, R., Hand, J., and Avise, J.: Characterization of speciated
1075   aerosol direct radiative forcing over California, J. Geophys. Res. Atmos., 118, 2372–2388,
1076   doi:10.1029/2012JD018364, 2013a.

1077 Zhao, P., Zhou, X., Chen, J., Liu, G., and Nan, S.: Global climate effects of summer Tibetan
1078   Plateau, Science Bulletin, 64, 1–3, doi:10.1016/j.scib.2018.11.019, 2019.

1079 Zhao, Z., Cao, J., Shen, Z., Xu, B., Zhu, C., Chen, L. W. A., Su, X., Liu, S., Han, Y., Wang,
1080   G., and Ho, K.: Aerosol particles at a high-altitude site on the Southeast Tibetan Plateau,
1081   China: Implications for pollution transport from South Asia, J. Geophys. Res. Atmos., 118,
1082   11,360-11,375, doi:10.1002/jgrd.50599, 2013.

1083 Zhong, S., Qian, Y., Zhao, C., Leung, R., Wang, H., Yang, B., Fan, Ji., Yan, H., Yang, X., and
1084   Liu, D.: Urbanization-induced urban heat island and aerosol effects on climate extremes in
1085   the Yangtze River Delta region of China, Atmos. Chem. Phys., 17, 5439–5457,
1086   doi:10.5194/acp-17-5439-2017, 2017.

1087
1088
1089
1090
1091
1092
1093

Table 1. Summary of model configurations.

Description	Selection	References
Horizontal grid spacing	20 km (D1),4 km (D2)	
Grid dimensions	250×350, 300×400	
Topography	30 arcsec (USGS)	
Vertical layers	54 (roughly 17 layers below 2 km)	
Model top pressure	50 hPa	
Nesting approach	One-way	
Aerosol scheme	MOSAIC 8 bin	Zaveri et al., 2008
Gas-phase chemistry	CBM-Z	Zaveri and Peters, 1999
Long wave Radiation	RRTMG	Iacono et al., 2000; Zhao et
Short-wave Radiation	RRTMG	al., 2011, 2013a
Cloud Microphysics	Morrison 2-moment	Morrison et al., 2009
Cumulus Cloud	Kain-Fritsch	Kain, 2004
Planetary boundary layer	MYNN level 2.5	Nakanishi and Niino, 2006
Land surface	CLM	Oleson et al., 2010
Meteorological Forcing	ERA-Interim, 0.5°×0.66°, 6 hourly	
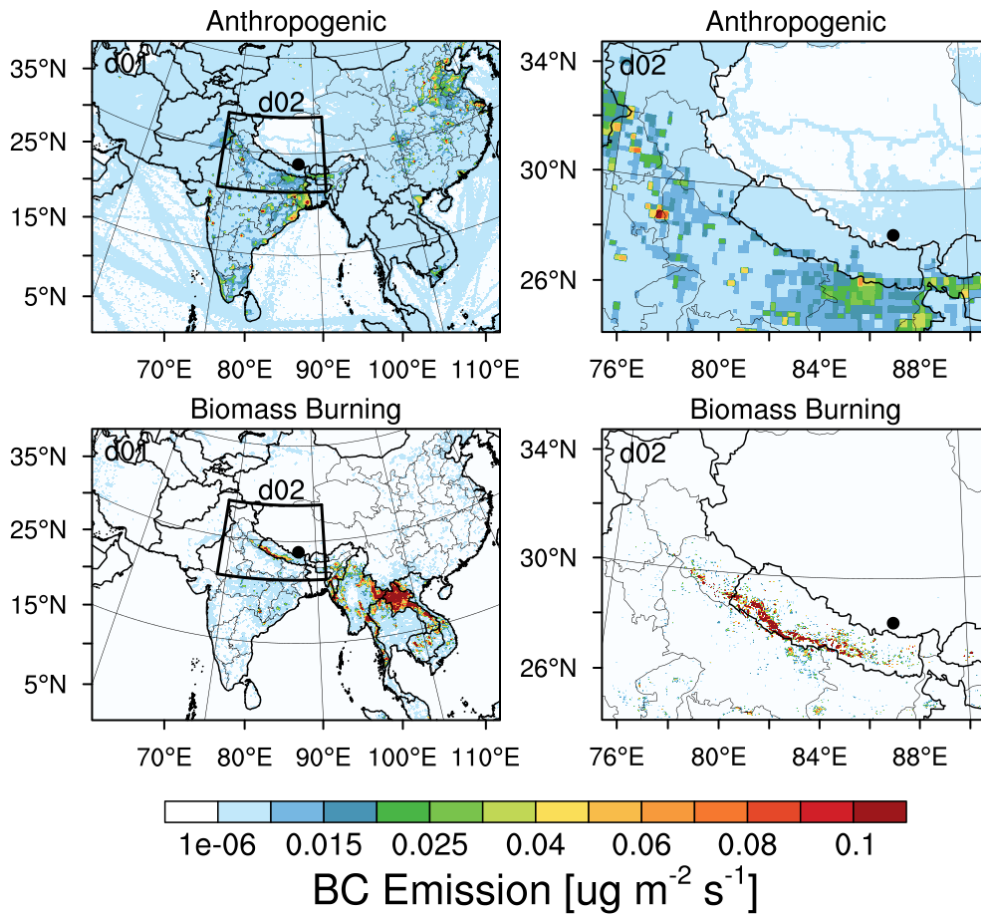
Figure 1. Anthropogenic and fire emissions over the entire simulated regions of 20 km and 4
km resolutions, the black dot represents the Qomolangma Station (QOMS).

1152
1153
1154
1155

1156
1157 **Figure 2.** The thickness of each vertical layer in the simulations (54 layers in total).
1158
1159
1160
1161
1162
1163
1164
1165
1166
1167
1168
1169
1170
1171
1172
1173
1174

1175
1176
1177
1178

1179
1180 **Figure 3.** Spatial distributions of terrain height from the dataset at 20 km (Smooth Topo) and
1181 4 km (Complex Topo) resolutions. The one dash line and two solid lines represent the cross
1182 sections for analysis in the following.

1183
1184
1185
1186
1187
1188
1189
1190
1191
1192
1193
1194
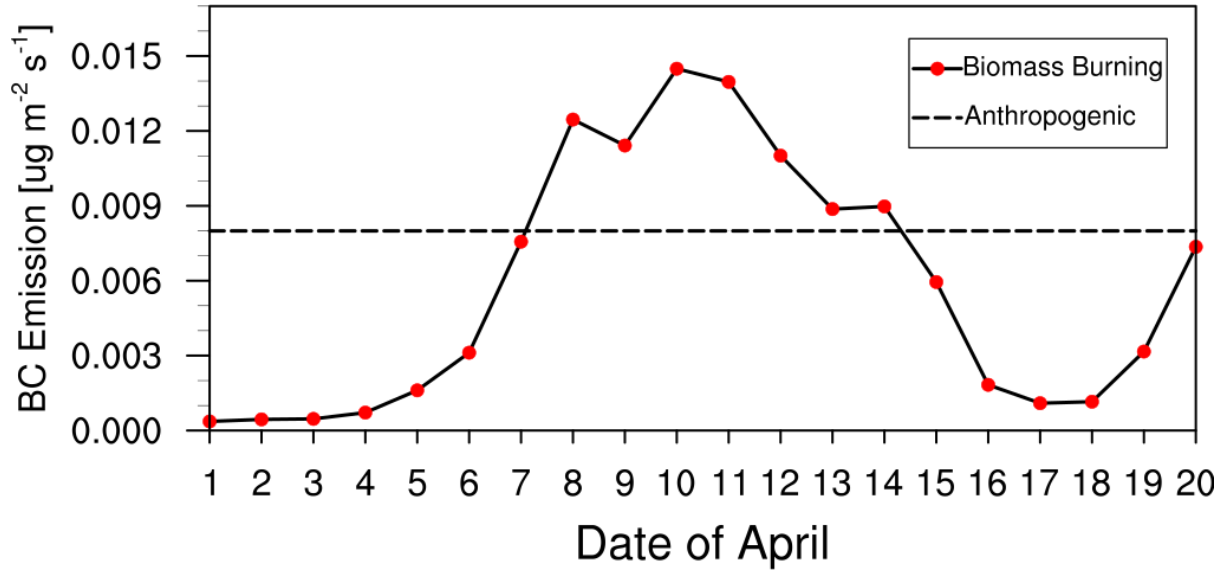
Figure 4. Time series of area-averaged daily fire emissions between 26°N and 29°N over the
simulation domain at 4 km resolution (The dash line in the figure represents the anthropogenic
emissions).

1231
1232
1233
1234
1235

Figure 5. Spatial distributions of column integrated BC mass and the wind field at 500 hPa
from the simulations with complex and smooth topography (Complex Topo and Smooth Topo)
averaged for April 1-20, 2016. The difference between the two is also shown.
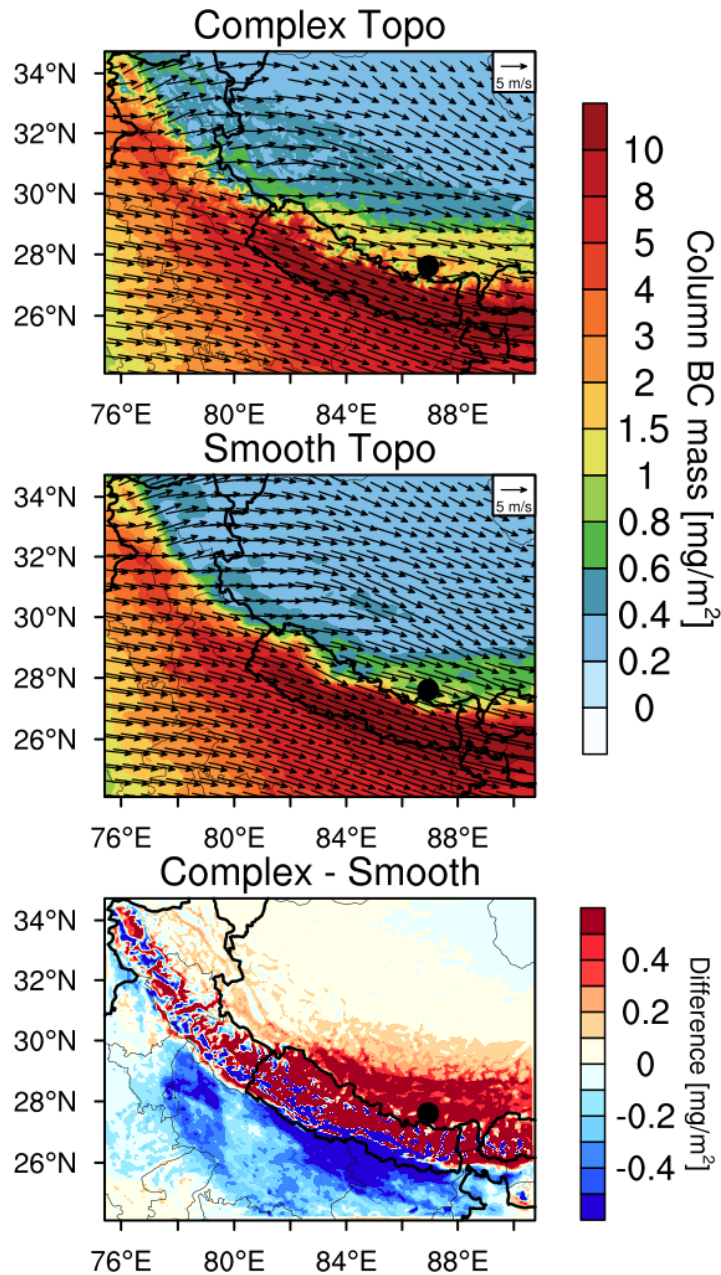
1240
1241
1242
1243
1244
1245
1246
1247

1248
1249
1250
1251

1252
1253 **Figure 6.** Spatial distributions of AOD from the MODIS retrievals and the simulations with
1254 complex and smooth topography averaged for April 1-20, 2016. The two black dots represent
1255 the two AERONET sites over the TP (QOMS, 86.94°E, 28.36°N; NAM, 90.96°E, 30.77°N).
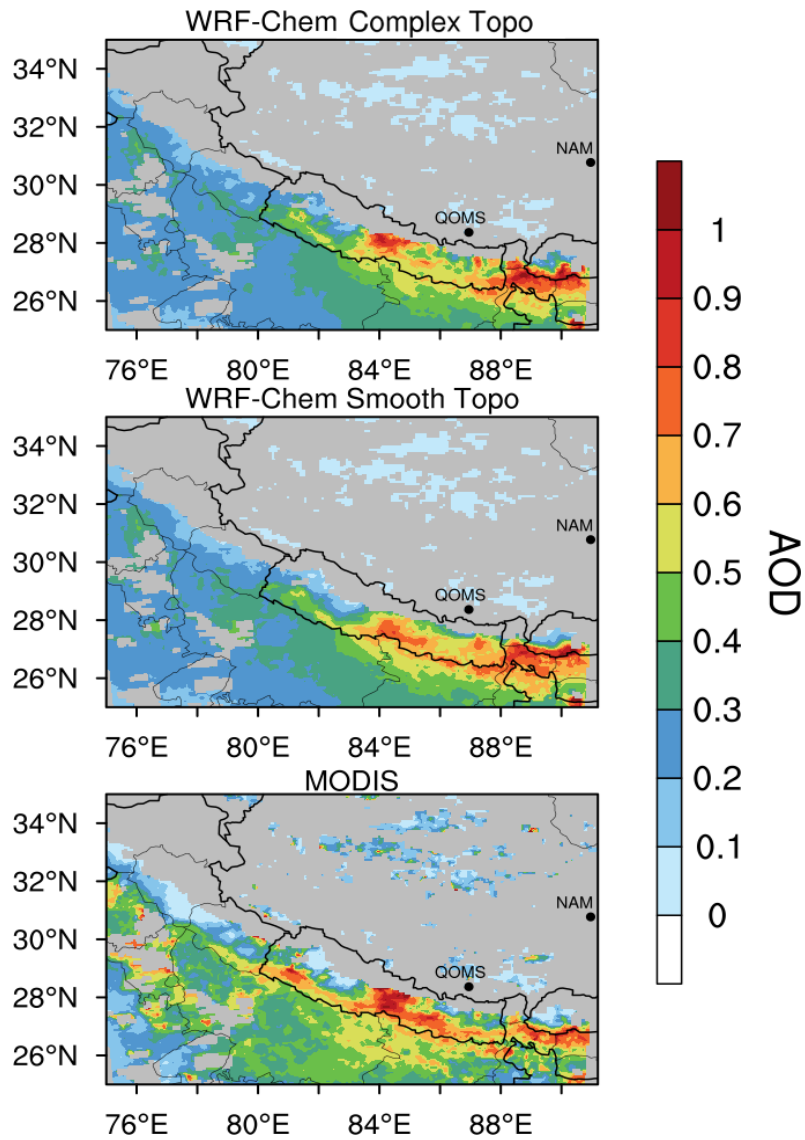
1256
1257
1258
1259
1260
1261
1262
1263
1264
1265
1266
1267
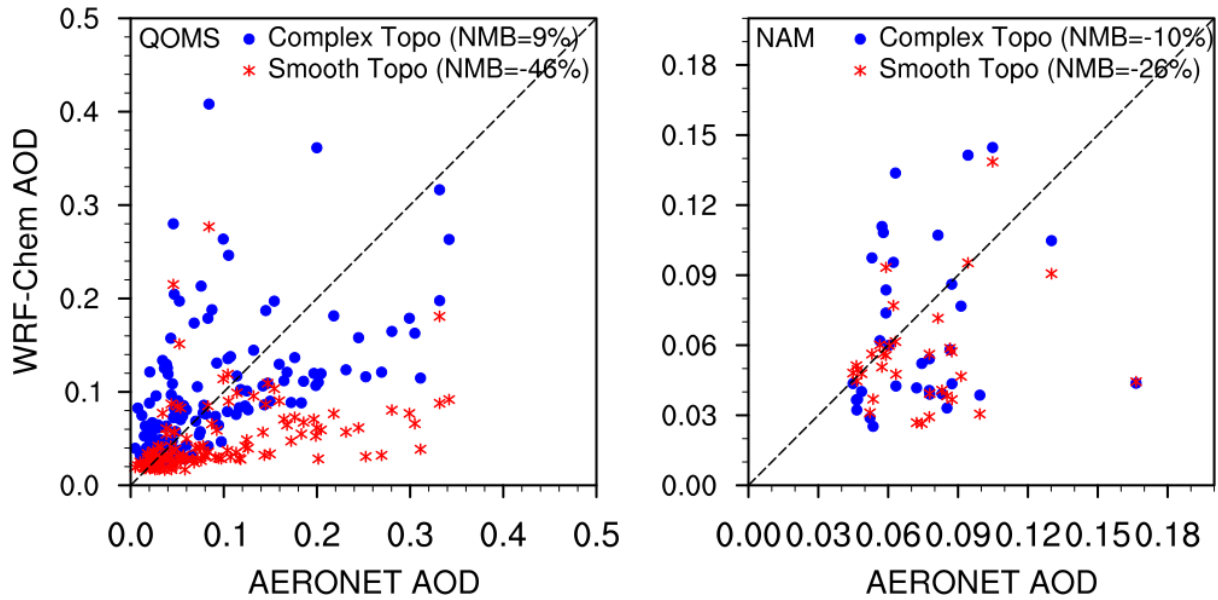
1276
Figure 7. Hourly AOD from the measurements of AERONET and simulations by WRF-Chem
1277 at the two sites over the TP (QOMS, 86.94°E, 28.36°N; NAM, 90.96°E, 30.77°N) for April 1-
1278
1279 20, 2016.

1302
1303
1304
1305
1306
1307
1308
1309
1310
1311
1312
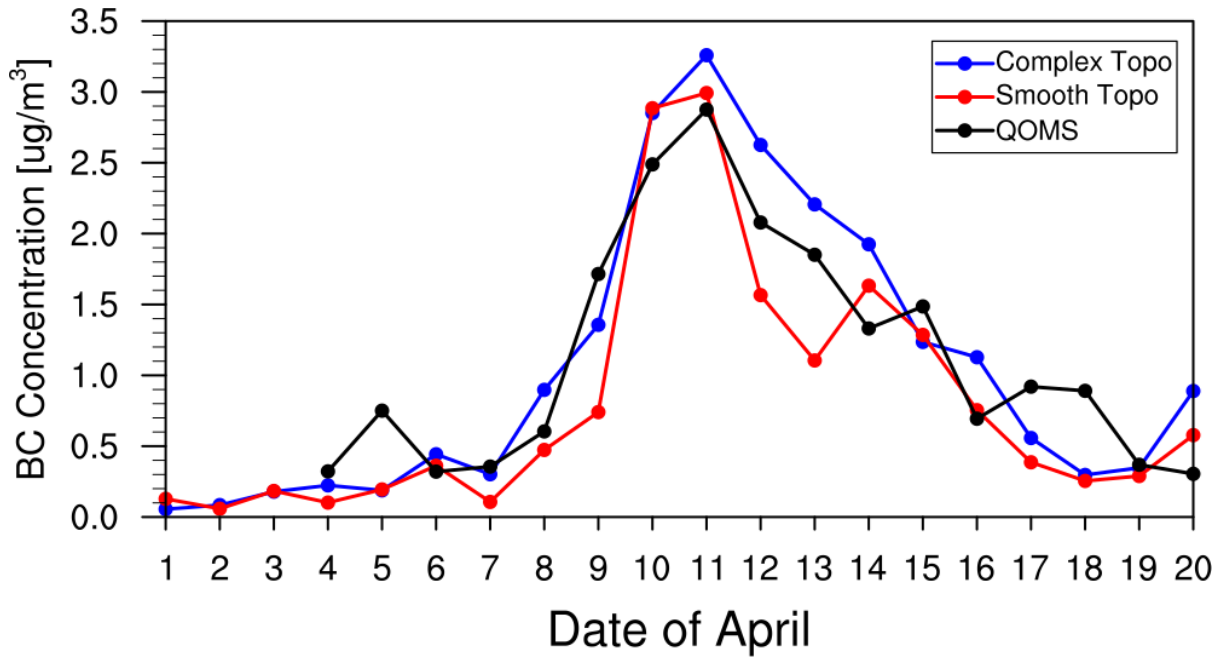
1313
1314 **Figure 8.** The simulated (colored) and observed (black) temporal variability of surface BC
1315 mass concentration at the measurement station during April 1-20 in 2016.
1316
1317
1318
1319
1320
1321
1322
1323
1324
1325
1326
1327
1328
1329
1330
1331
1332
1333
1334
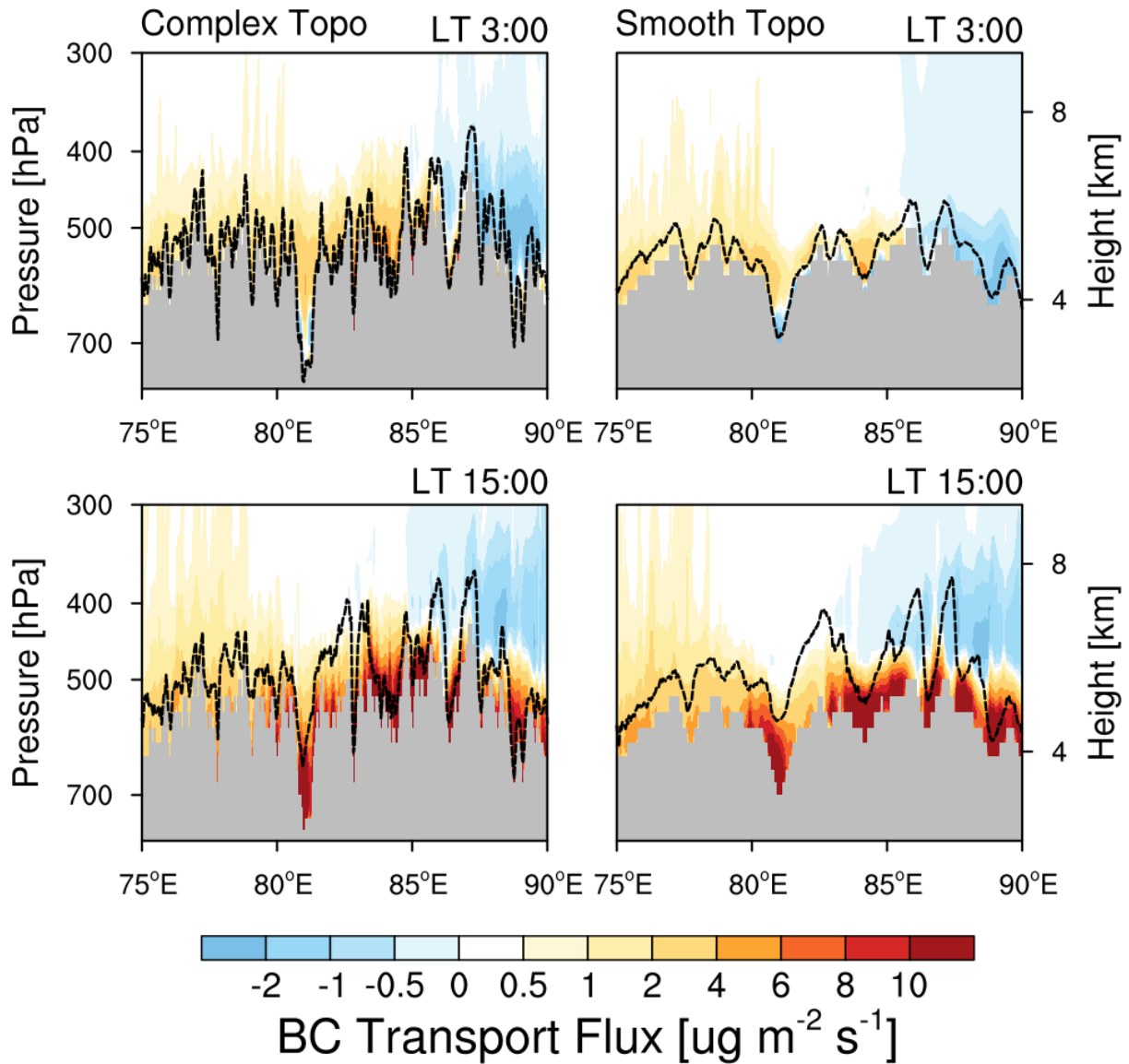
Figure 9. Longitude-height cross section of BC transport flux along the cross line (shown as the black dash line in Fig. 3) from the simulations with complex and smooth topography at local time (LT) 03:00 and 15:00 averaged for April 1-20. The PBL height along the cross section is shown here as the black dash line.

1355
1356
1357
1358
1359
1360
1361
1362
1363
1364
1365

Figure 10. Latitude-height cross section of BC flux (vector) across the mountain (shown as the
East black solid line in Fig.3) from the simulations with complex and smooth topography at
local time (LT) 03:00 and 15:00 averaged for April 1-20, 2016. Contour represents the BC
concentration.
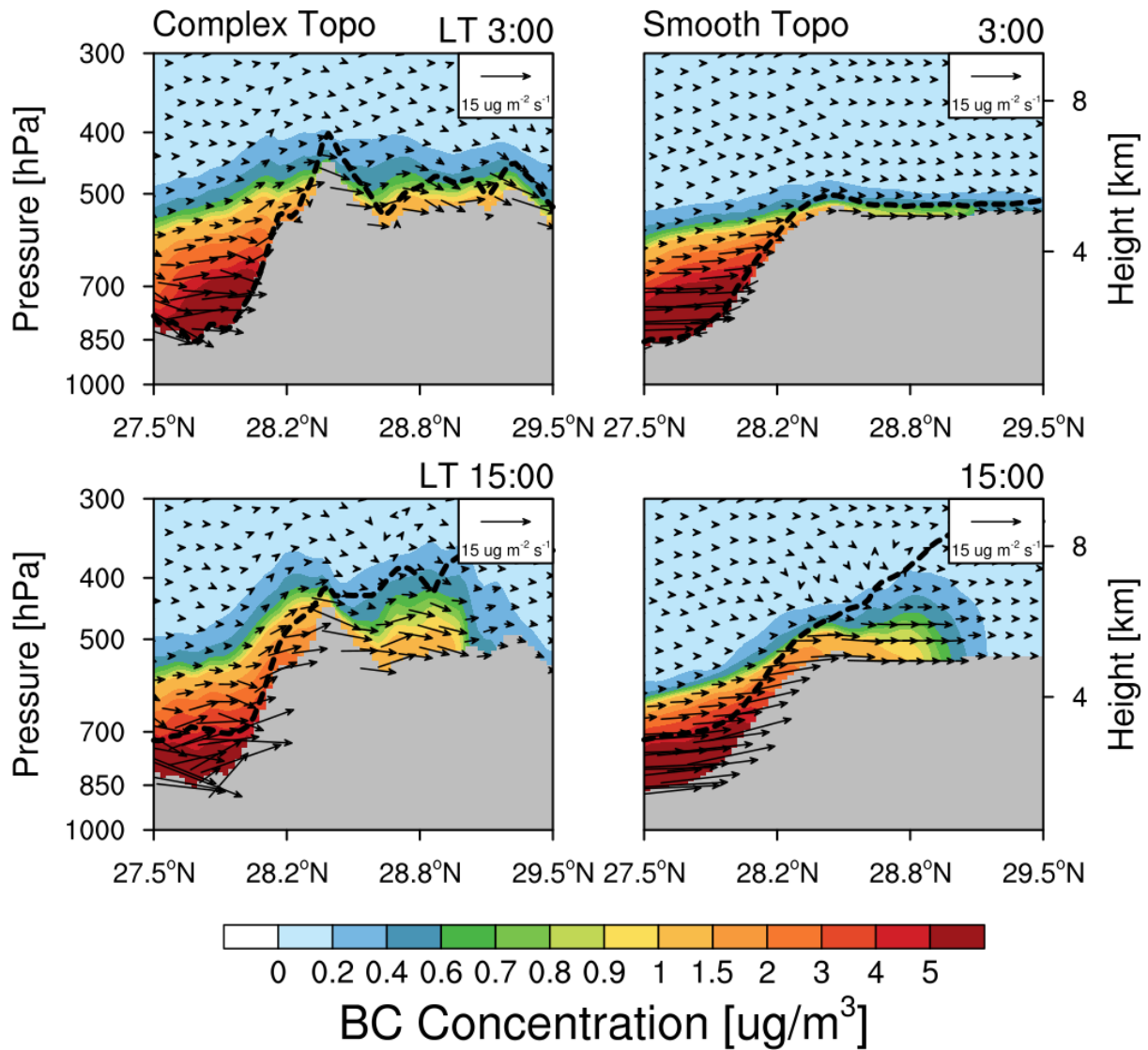
1371
1372
1373
1374
1375
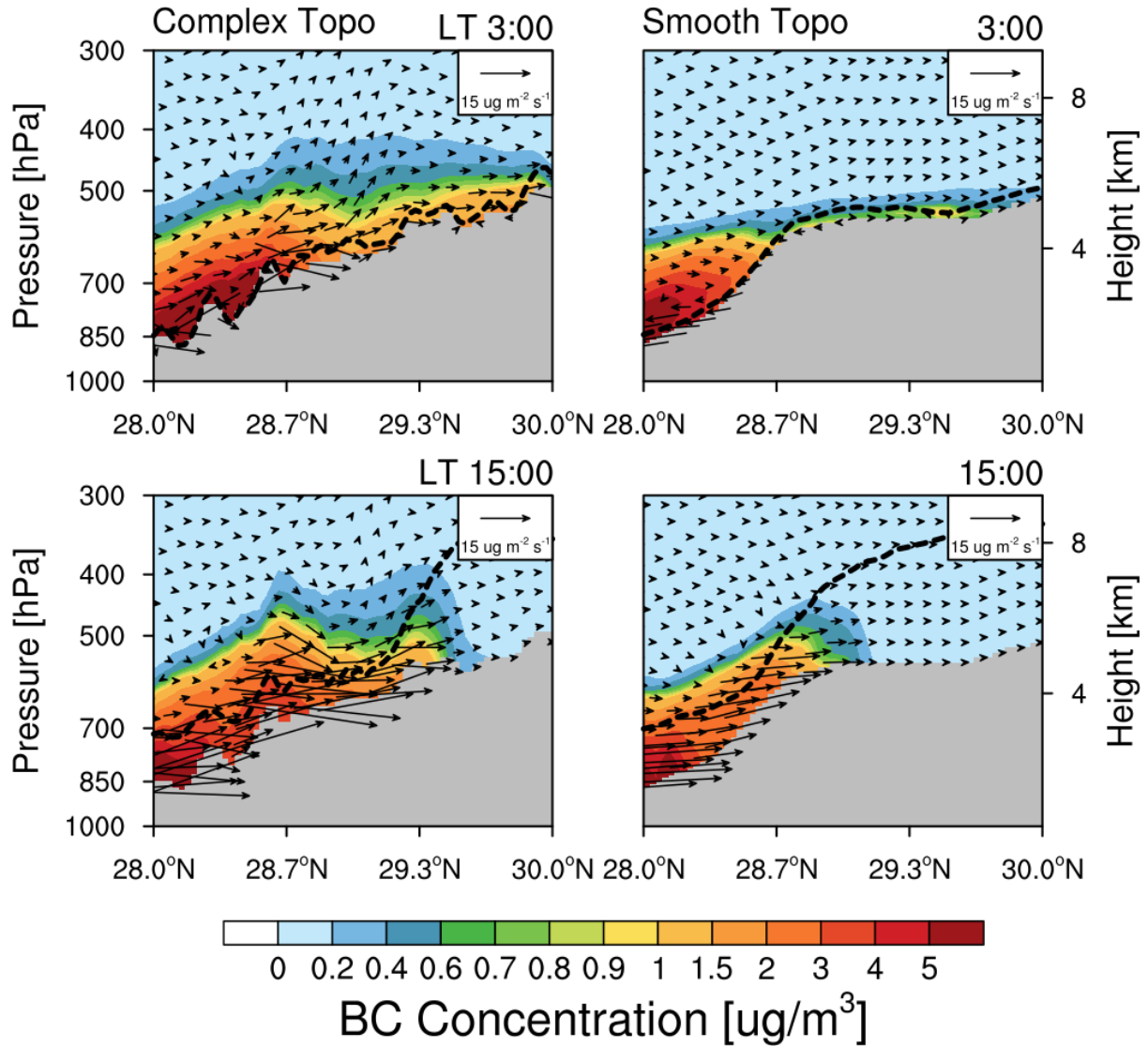
Figure 11. Latitude-height cross section of BC flux (vector) along the valley (shown as the
West black solid line in Fig. 3) from the simulations with complex and smooth topography at
local time (LT) 03:00 and 15:00 averaged for April 1-20, 2016. Contour represents the BC
concentration.

1397
1398
1399
1400
1401
1402
1403

Figure 12. Longitudinal distribution of integrated BC mass flux along the cross section in Fig. 3 from the simulations with complex and smooth topography. The black lines represent the terrain heights with different topography.
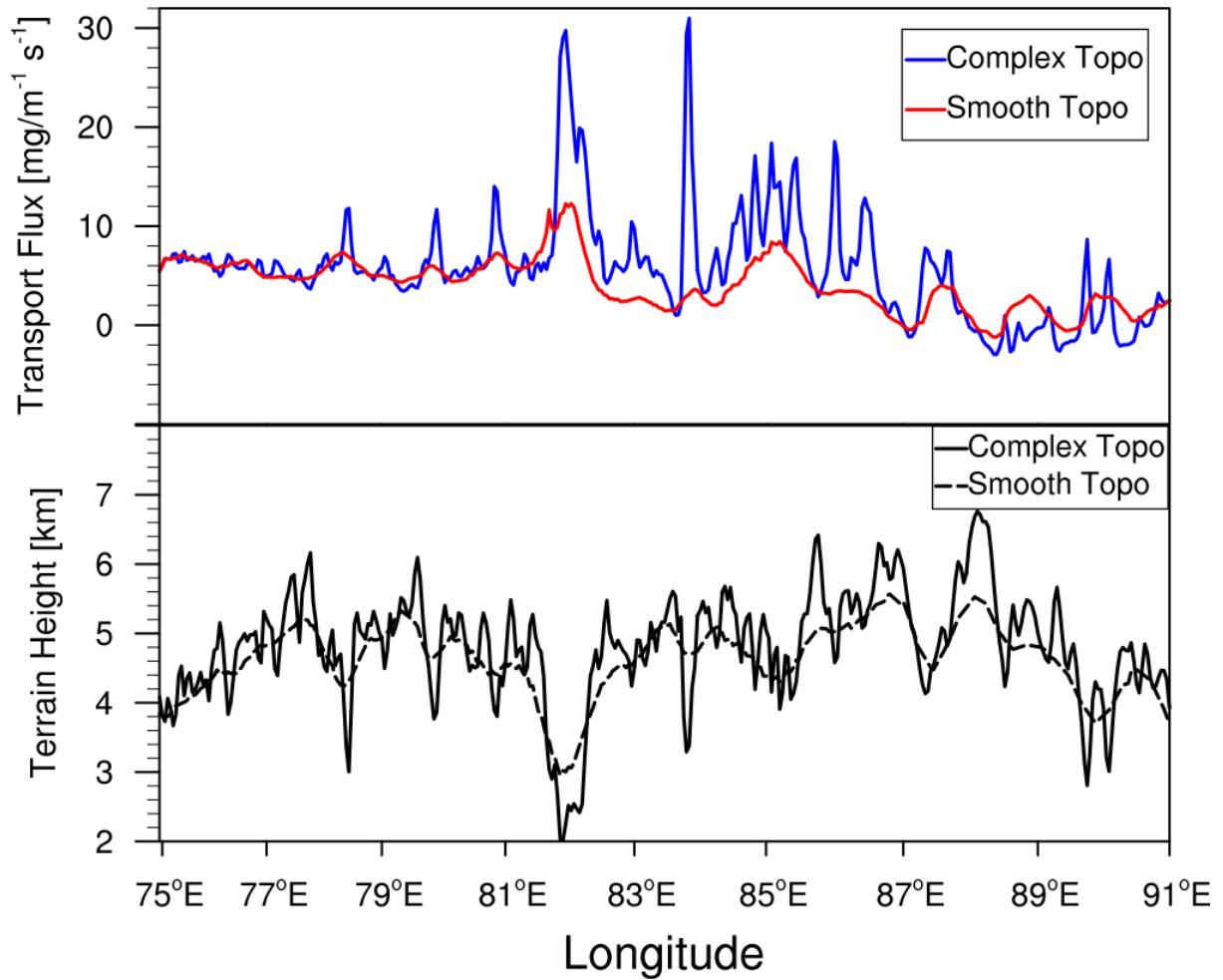
1404
1405
1406
1407
1408
1409
1410
1411
1412
1413
1414
1415
1416
1417
1418
1419
1420
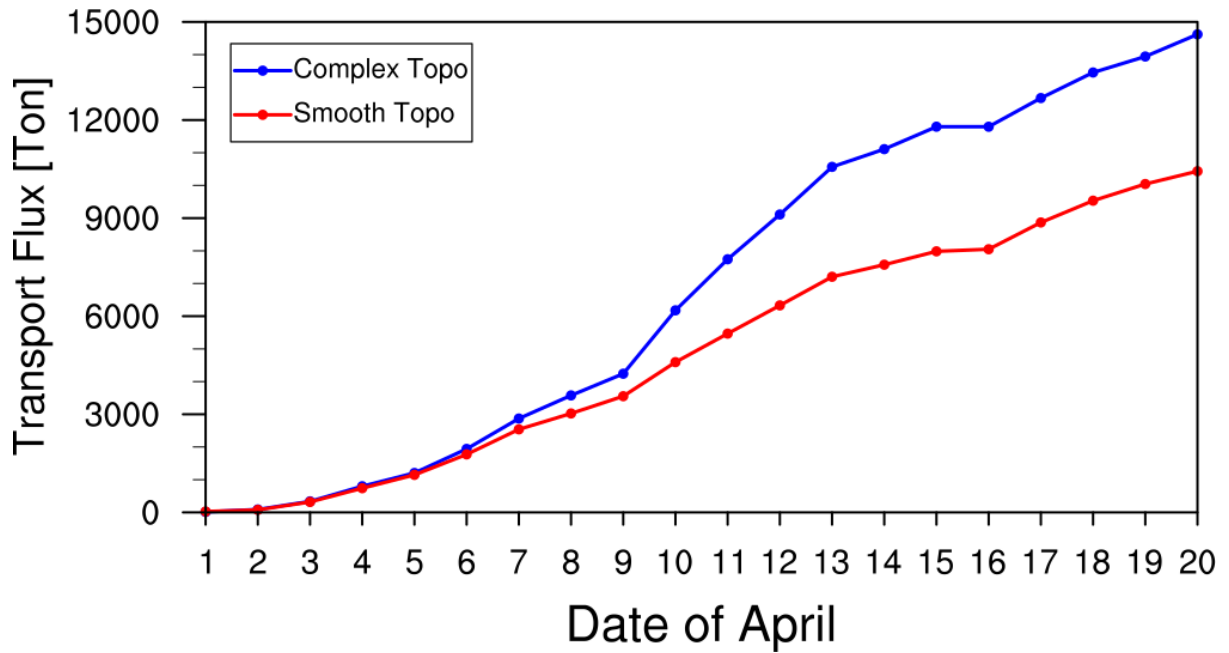
1429
Figure 13. Accumulated integrated total transport flux of BC across the Himalayas estimated from the simulations with complex and smooth topography during April 1-20, 2016.

1455
1456
1457
1458
1459

1460
1461 **Figure 14.** Vertical profiles of BC induced radiative heating rate in the atmosphere averaged
1462 over the TP (with elevation > 4 km) from the simulations with complex and smooth topography
1463 during April 1-20, 2016.
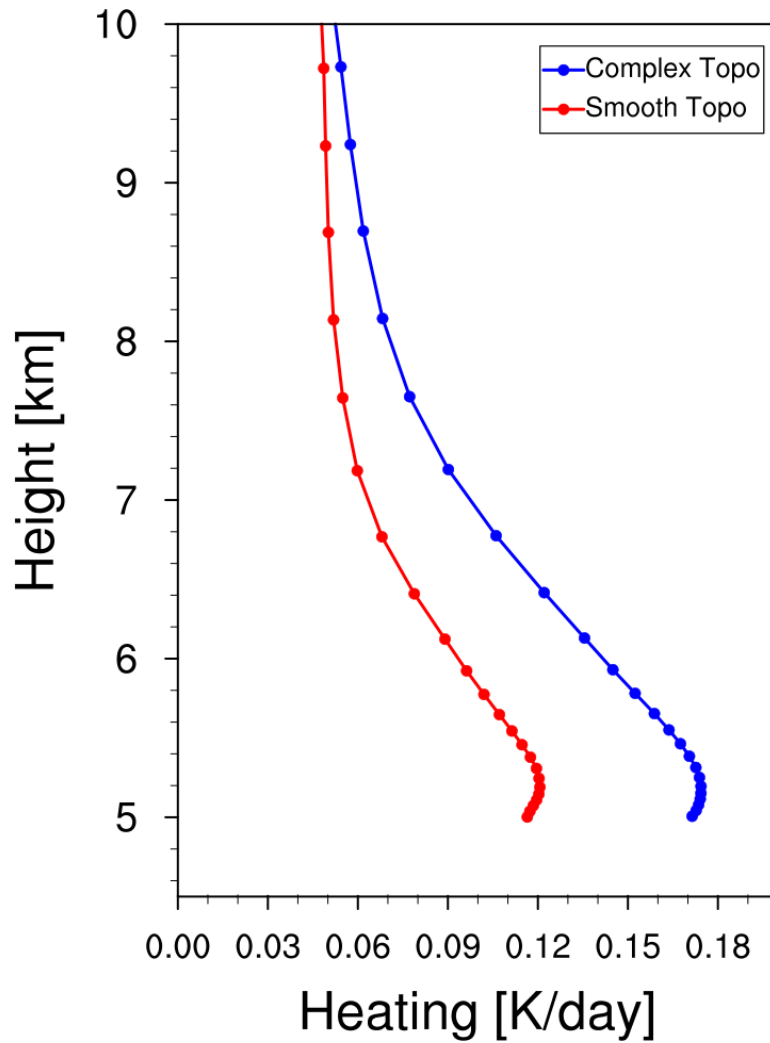
1464
1465
1466
1467
1468
1469
1470
1471
1472
1473
1474
1475
1476
1477
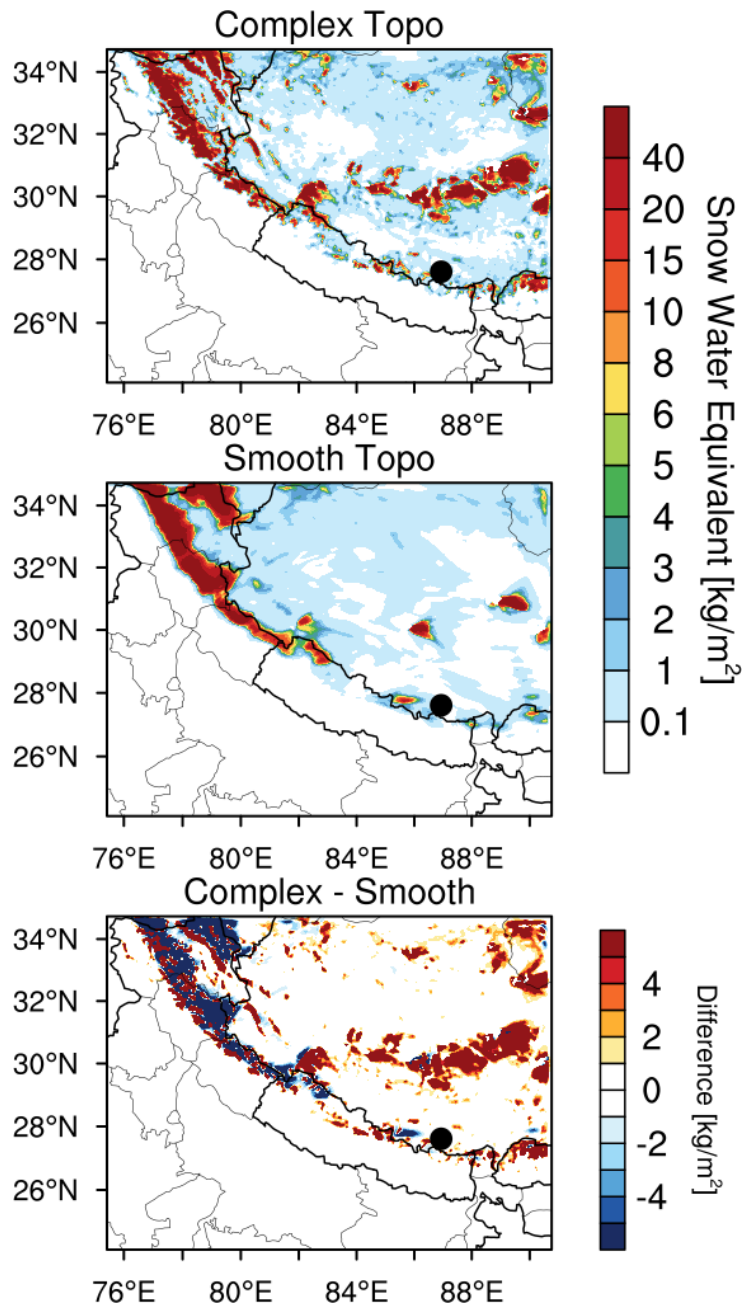
Figure 15. Spatial distributions of snow water equivalent averaged for April 1-20, 2016 from the simulations with complex and smooth topography. The difference between the two is also shown.

1494
1495
1496
1497

Figure 16. Spatial distributions of BC radiative forcing in the surface snow averaged for April 1-20, 2016 from the simulations with complex and smooth topography. The difference between the two is also shown.
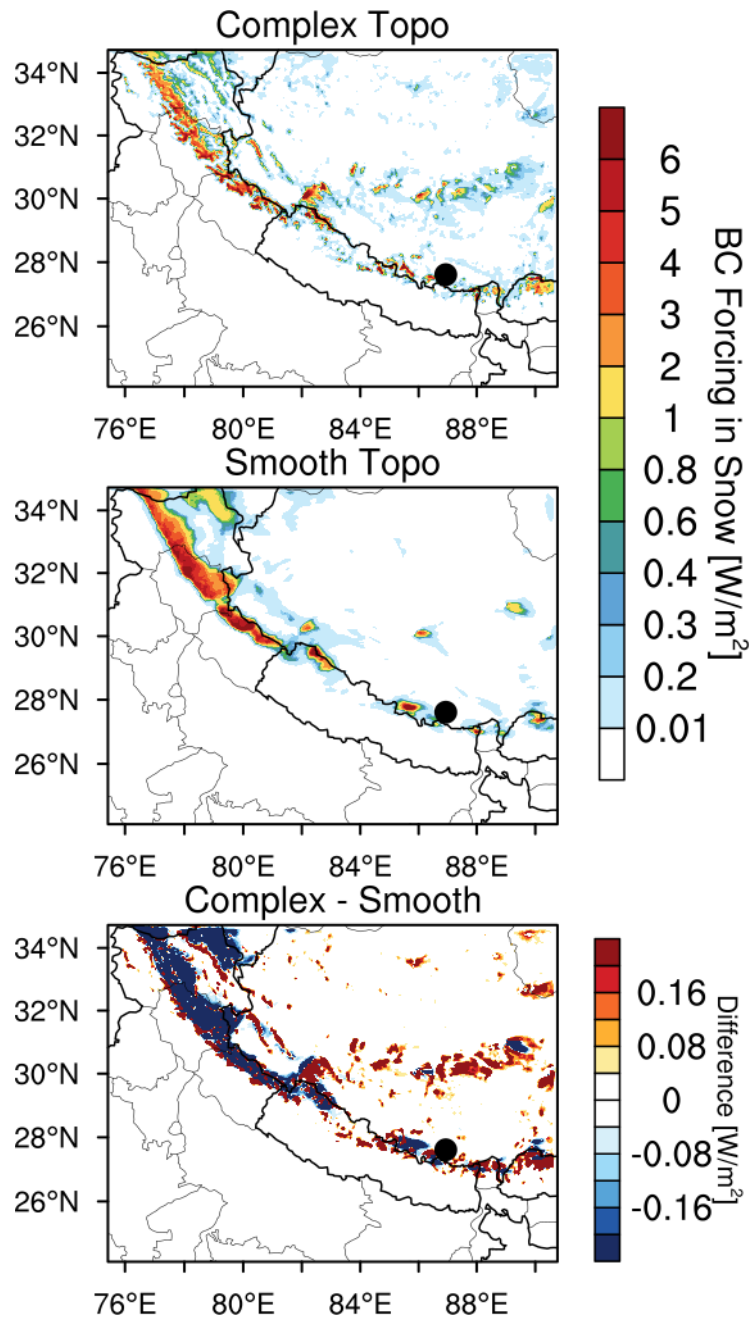
1498
1499
1500
1501

1502
1503
1504
1505